



**VNiVERSiDAD
D SALAMANCA**

CAMPUS OF INTERNATIONAL EXCELLENCE

**SPATIAL AND SPECTROSCOPIC CHARACTERIZATION
OF HIGH-RESOLUTION $\text{LaCl}_3(\text{Ce})$ CRYSTALS
COUPLED TO SILICON PHOTODETECTORS**

MsC DEGREE THESIS

MASTER INTERUNIVERSITARIO EN FISICA NUCLEAR

Author:

Pablo Olleros Rodríguez

Tutors:

PhD. Luis Caballero Ontanaya, IFIC-Universitat de València

PhD. César Domingo-Pardo, IFIC- Universitat de València

PhD. David Rodríguez Entem, Universidad de Salamanca

This project was developed within the HYMNs Project and was funded by the European Research Council (ERC) under the Europeans Union's Horizon 2020 research innovation programme (grant agreement No. 681740)

We acknowledge support from the Spanish research project FPA2017-83946-C2-1-P.

INDEX

ABSTRACT/RESUMEN	5
1.- INTRODUCTION	7
2.- THEORETICAL BACKGROUND	9
2.1.- STELLAR NUCLEOSYNTHESIS.	9
2.2.- NEUTRON CAPTURE. THE S-PROCESS.	11
2.3.- MEASUREMENT OF NEUTRON CAPTURES RATES	16
2.3.1 PULSED NEUTRON SOURCES	16
2.3.2.- NEUTRON CAPTURE DETECTORS	17
A.-Total absorption calorimeters	17
B.- Total energy detectors.....	17
3.- THE i-TED CONCEPT	19
3.1.- STATE-OF-THE-ART AND SCIENTIFIC MOTIVATION.....	19
3.2.- i-TED DESCRIPTION	20
3.3.- COMPTON IMAGING	22
4.- ITED POSITION SENSITIVE DETECTORS: PERFORMANCE CHARACTERIZATION AND OPTMIZATION	25
4.1.- EXPERIMENTAL APPARATUS AND METHODOLOGY	25
4.1.2- Scintillation crystals.....	25
4.1.2- Photosensors.....	26
4.1.3- Power and readout electronics.....	28
A.- PMT Assembly.....	28
B.- SiPM assembly	29
4.2.- SPECTROSCOPIC PERFORMANCE. MEASUREMENTS	29
4.3.- MONTECARLO SIMULATIONS	31
4.3.1.- GEANT4	32
A.- SIMULATION DESCRIPTION.....	32
B.- OPTICAL PHYSICS.....	34
C.- MULTITHREAD MODE	37
4.3.2.- ROOT	37
5.- RESULTS.....	39
5.1.- CODE VALIDATION	39
5.2.- ENERGY RESPONSE.....	41
5.2.- SPATIAL RESPONSE.....	42
5.2.1.- XY RESPONSE.....	44

A.- ANGER TECHNIQUE.....	44
B.- PANI TECHNIQUE	46
5.2.2.- DEPTH OF INTERACTION	49
6.- CONCLUSIONS/CONCLUSIONES	51
APPENDIX A. DATA ANALYSIS SCRIPTS.....	54
A.1 PMTModel.C	54
A.2 SiPMMModel.C.....	55
A.3 processing.C	57
A.4 spatialResponseAnger.c.....	62
A.5 spatialResponsePani.C	64
A.6 fitLerche.C.....	66
FIGURE INDEX.....	68
BIBLIOGRAPHY.....	71

ABSTRACT

The neutron-capture s-process plays a major role in the synthesis of elements heavier than iron (^{56}Fe). Accurate measurements of (n,γ) cross-sections have revealed themselves as a crucial information source for a better understanding of stellar nucleosynthesis, which in turn, serves as an information source about physical properties that dictate galactic and stellar evolution. Neutron-capture cross-sections have been measured over the last 50 years for several isotopes with available detection systems, however, the nature of neutron-capture experiments impose several constraints in order to measure many radioactive isotopes cross-sections that are of pivotal importance in order to understand the thermodynamic conditions where s-process takes place. To overcome this limitations, a new detection system has been proposed consisting on a total energy detector with imaging capabilities, so called i-TED. γ -Imaging capabilities are based on Compton's law and, in order to exploit this principle, the development of position sensitive detectors with both high energy and spatial resolution is required. In this work we explore the energy and spatial response of the position sensitive detectors proposed to be the basic element of the i-TED detection system. After a brief introduction, in section Sec.2 we will describe the historical background concerning stellar nucleosynthesis and s-process models. In section Sec.3, the scientific motivation that led to the proposal of the i-TED detector is exposed along with a detailed description of the solutions adopted in its development. The methodology followed and the experimental apparatus used to carry out the present work is exposed in section Sec.4. The results obtained with the study made are presented in section Sec.5 and in section Sec.6 we will give a brief summary and discussion of the work done along with a description of further studies that may be done in order to optimize i-TED's performance.

KEYWORDS: Nucleosynthesis, s-process, total energy detector, Compton imaging, position sensitive detector, scintillation crystal, silicon photomultiplier, Monte Carlo technique, optical simulation.

RESUMEN

El proceso-s de captura neutrónica juega un papel importante en la síntesis de elementos más pesados que el hierro (^{56}Fe). Medidas precisas de la sección eficaz de reacciones tipo (n,γ) se han revelado como una fuente de información crucial para un mejor entendimiento de la nucleosíntesis estelar que a su vez sirve como fuente de información de las condiciones físicas que dictan la evolución galáctica y estelar. Durante los últimos 50 años, se han llevado a cabo medidas de secciones eficaces de capturas neutrónicas para varios isotopos con los sistemas de detección que estaban disponibles. Sin embargo, la naturaleza de los experimentos de captura neutrónica impone serias restricciones a la hora de realizar medidas precisas de éstas secciones eficaces en isótopos radioactivos que tienen una importancia fundamental a la hora de entender las condiciones termodinámicas en las que se da el proceso s. Para superar estas limitaciones, un nuevo sistema de detección basado en la incorporación de capacidades de visualización gamma a un detector de energía total, llamado i-TED, ha sido propuesto. Las capacidades de visualización se basan en la aplicación de la ley de dispersión Compton que, para poder ser explotada, requiere el uso de detectores sensibles a la posición con una alta resolución tanto espacial como energética. En este trabajo exploramos la respuesta espectroscópica y espacial de los detectores sensibles a la posición que han sido diseñados como elementos básicos en el desarrollo de i-TED. Tras una breve introducción, en la sección Sec.2 expondremos el contexto histórico concerniente a la nucleosíntesis estelar y al proceso s de captura neutrónica. En la sección Sec.3 daremos la motivación científica que llevó al diseño de i-TED junto a una descripción de éste y de las soluciones adoptadas para su desarrollo. La metodología seguida en el desarrollo del trabajo junto a una descripción de los aparatos y herramientas usadas a lo largo del mismo se explicarán en la sección Sec.4. Los resultados obtenidos a lo largo del desarrollo del trabajo se expondrán en la sección Sec.5 y en la sección Sec.6 se desarrollará un breve resumen del trabajo junto a la discusión de los resultados y una descripción de futuros estudios que se pueden llevar a cabo en el desarrollo de i-TED.

KEYWORDS: Nucleosíntesis, proceso-s, detector de energía total, visualización Compton, detector sensibles a la posición, cristal de centelleo, fotomultiplicador de silicio, técnica Monte Carlo, simulación óptica.

1.- INTRODUCTION

Over the last decades important advances had been achieved both in radiation detectors and neutron-beam facilities, leading to accurate (n,γ) cross sections measurements and thus enabling the discovery of new facets of s-process nucleosynthesis and giving rise to a refinement of theoretical models of stellar and galactic chemical evolution. Regarding the experimental methodology, a large progress has been made from the first Moxon-Rae detectors developed in the sixties [1], which were soon afterwards replaced by organic C₆F₆ liquid scintillation total-energy detectors, and later by low neutron sensitivity C₆D₆ detectors [2] [3]. One of the main constraints found while developing new neutron-capture measurement systems is related to neutron-induced gamma-ray backgrounds, in order to minimize this effect, the most used approach consists on using total energy detectors (TED) along with the use of the pulse-height weighting technique (PHWT) [2] [4].

With the aim of exploring new ways of improving this situation, the possibility of using low-efficiency radiation detectors with gamma-ray imaging capability, so called i-TED [5], combined with the PHWT is being investigated within the European Research Council granted project HYMNS (High sensitivity Measurements of key-stellar NucleoSynthesis reactions). Building on a previous successful experiment based on a mechanically collimated gamma-camera [6], a new electronically collimated gamma-imager i-TED prototype is being developed in order to perform first proof-of-principle measurements at CERN n_TOF (neutron Time-Of-Flight facility) [7]. The new detection system is based on the Compton Scattering law which provides a way of finding, on an event-by-event basis, a cone representing the geometrical points of the Euclidean 3D space which are susceptible of containing the radiating source and thus, being able to reject a large of the extent background gamma-rays originating from contaminant neutron capture events in the surroundings of the capture sample.

The use of Compton's principle requires of excellent energy-, spatial-, and time resolution for the detecting system. Recent experimental studies have reported promising results for lanthanum halide crystals coupled to silicon photomultipliers (SiPMs) [8] [9]. However, for their implementation in neutron capture experiment, two additional features need to be considered, namely, i) the use of materials with low neutron sensitivity to keep the intrinsic prompt-capture background as low as possible, and ii) the use of large monolithic crystals in order to enhance detection efficiency and thus keep the overall experiment beam-time within reasonable limits.

In this work, we will explore the spectroscopic performance of large area monolithic LaCl₃(Ce) crystals of several thicknesses, coupled to pixelated silicon photomultipliers. Such kind of position sensitive detectors (PSDs) will be the main building elements of the aforementioned i-TED prototype. For our application, on one side, a thin pixel granularity leads to a more accurate sampling of the scintillation light-distribution and, in principle, this might lead to a better position reconstruction. On the other hand, the higher dead-space related to the high granularity also implies a loss of scintillation photons and thus, a deterioration of the energy response which needs to be quantified. Therefore, an optimal pixel granularity needs to be found for the best trade-off between energy- and position-resolution, while keeping under reasonable levels the scalability and complexity of the system.

In order to study these aspects, we have carried out a Monte Carlo (MC) study of the PSDs themselves, which includes both electromagnetic gamma-ray physics and optical interactions for all scintillation photons generated in each gamma-ray interaction inside the crystal. This allows us to study, in a rather realistic fashion, the energy- and position-response of the PSDs. The results obtained from these calculations are experimentally validated by means

of a series of benchmark measurements carried out in the laboratory, both with a conventional mono-cathode PMT and a pixelated SiPM. After validation of our computation model, we will use it to infer the optimal pixel size for a trade-off between energy- and 3D position-resolution. Results obtained along with the comparisons of the measurements that had been made and a possible further analysis that may be useful for the i-TED development will be finally shown.

2.- THEORETICAL BACKGROUND

In this section we will expose the theoretical basis needed for a better comprehension of the context of this project, the working principle of the i-TED prototype and the features used to exploit the detector capabilities.

2.1.- STELLAR NUCLEOSYNTHESIS.

At the first half of the 20th century the first studies trying to estimate the abundances of the different elements conforming the universe were carried out [10] [11] [12], and were of such importance to understand which mechanisms were beneath the synthesis of the different nuclei observed. The first attempt to describe the mechanism that led to the universe nuclei distribution was made by Gamow, Alpher and Herman [13] who postulated that the elements of the universe were created in a primordial state of the universe, i.e. short time after the Big Bang¹. Other authors also worked on this [14]. A change of paradigm was triggered by the first observation of Technetium in red-giant stars by S.Paul Merrill in 1952 [15]. Technetium has no stable isotope, being the longest lived ⁹⁸Tc, with a half-life of 4 million years, which is too short for this element to be present at the stellar birth. In 1957, the first quantitative theory about stellar nucleosynthesis came to light [16] [17]. In the so called B²FH paper, a new theory was established rejecting the initial idea of heavy elements nucleosynthesis in the Big Bang and proposing that inside the stars we could find proper thermodynamic conditions that lead to the synthesis of all the elements on the basis of Hydrogen and Helium nuclear reactions. The authors arrived to this conclusion studying precisely the schematic curve of atomic abundances in the universe² and they were able to give an explanation to every detail shown in the distribution as can be seen in Fig. 1.

¹ At this time, the so-called *proton-proton chain* [59] and the *CNO cycle* [60] [61] were derived to account for the energy production within the stars, however, these fusion theories couldn't explain how to synthesize elements heavier than Helium, this led to the interpretation that all elements should be residual from the Big Bang.

² Synthesis of heavier elements also requires a bigger time scale than that where the thermodynamic conditions described in the Gamow Teller theory took place.

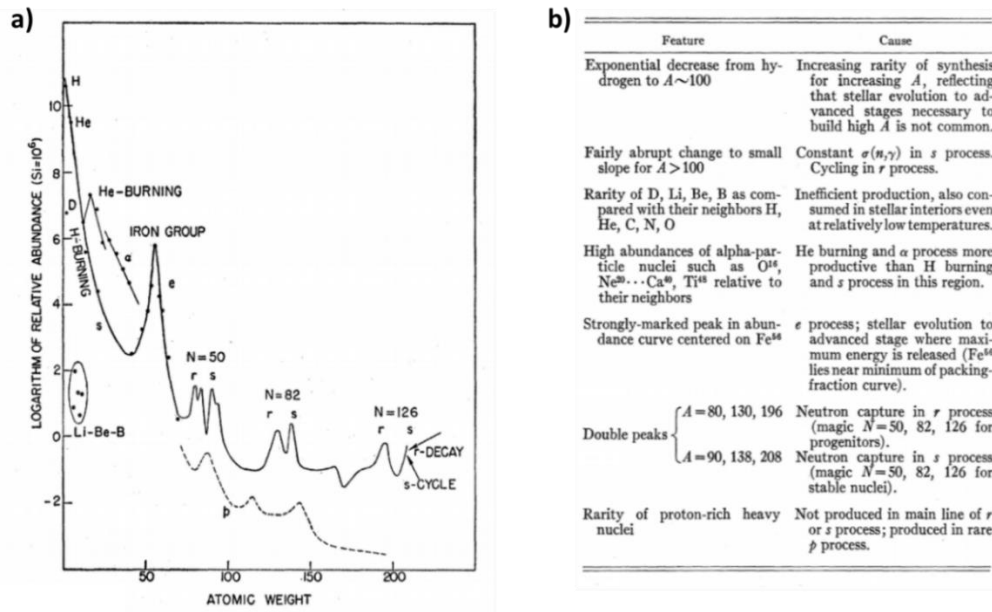


Fig. 1.- a) Curve of atomic abundances as a function of atomic weight based on the data of Suess and Urey. b) Explanations given in the B²FH paper for the different features characterising the curve of atomic abundances.

Nowadays the most accepted theory is that lighter elements such as Hydrogen, Helium and Lithium were created short after the big bang, whereas heavier elements are synthesized in different stages of stellar and galactic evolution by means of different processes, as:

- Fusion (H-, He-, Li-, C-, Ne-, O-, Si-burning, α -processes).
- Proton capture (p- and rp-process)
- Neutron capture (r- and s- process)
- Photodisintegration.

These processes may take part in different stages, layers and generations of stars during their stellar evolution and depend on their surrounding thermodynamic conditions and the physical properties and reactions characteristics of the involved nuclei. In figure Fig.2 can be seen the origin of the elements forming the periodic table and the well-known Hertzsprung-Russell diagram that gives a better understanding of stellar evolution.

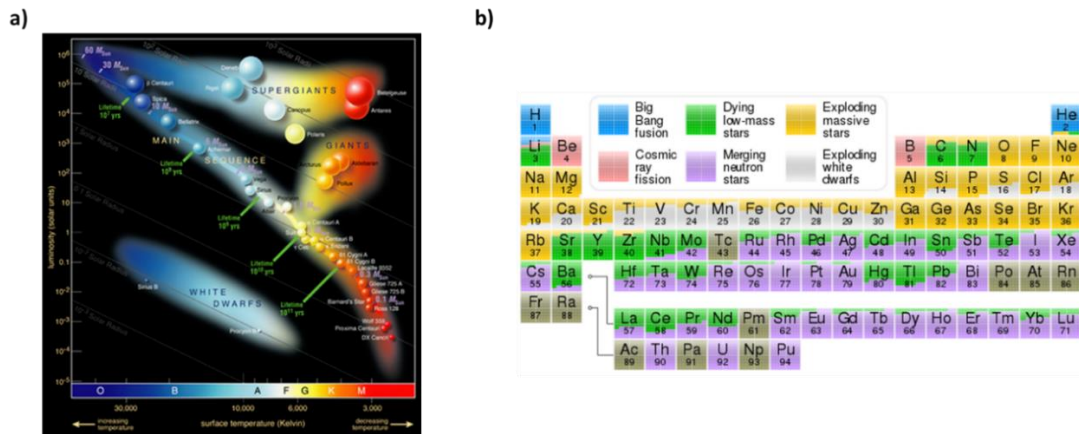


Fig. 2.- a) Scheme of stellar evolution reflected in the Hertzprung-Russell diagram. b) Origin of the elements of the periodic table due to the Big Bang and different type of stars.

The stars at the early stages reach hydrostatic equilibrium in a process by which the gravitational energy is balanced by fusion of light elements and hereby synthesizing heavier ones. By gravity, the heavy elements are accumulated in the core of the stars. Such burning processes have an upper limit represented by ^{56}Ni because this element has the highest binding energy per nucleon and thus, fusion cannot release more energy. From this point, the generation of heavier elements is achieved by means of nucleon-capture reactions and some of them also via photodisintegration processes, where a previously synthesized nucleus absorbs a high-energy gamma-ray ejecting a subatomic particle (neutron, proton or alpha particle).

2.2.- NEUTRON CAPTURE. THE S-PROCESS.

The absorption of a neutron or a proton by an atomic nucleus forms a new element or isotope³.



The fact that proton carries electric charge makes the second reaction in equation Eq. 1 much less probable to take place, as they feel electric repulsion. Thus, neutron capture reactions become the main source for the synthesis of elements heavier than iron. When a seed nucleus absorbs a neutron, a new isotope (placed at the right side of the seed nucleus in the nuclei chart) is created in an excited energy state which decays to the ground state by the emission of one or more gamma-rays. If the produced nucleus is unstable, it can therefore decay into another element via beta-decay processes. An example of a neutron capture reaction is shown in figure Fig. 3

³ The symbol * indicates that the resulting nuclei is placed on an excited energy state.

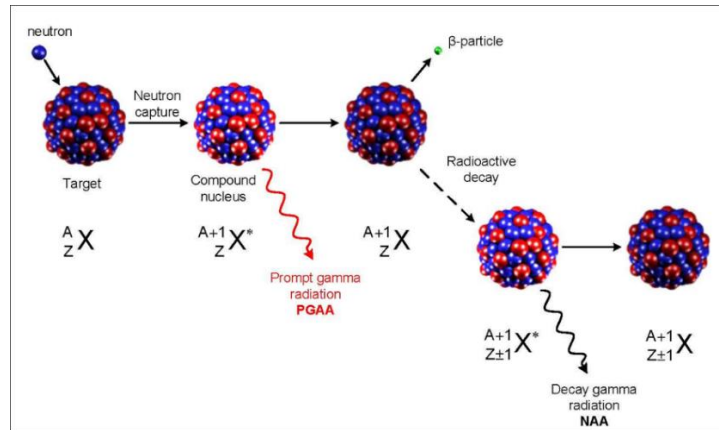


Fig. 3.- Neutron capture event with the subsequent emission of radiation due to the de-excitation of the resulting nucleus and its following β -decay.

The phenomenological picture of the stellar nucleosynthesis for the elements heavier than iron describes two different neutron capture processes. These are the so called r-process (rapid neutron-capture process) and the s-process (slow neutron-capture process)⁴. The main difference between r- and s-process resides in the time scale of the neutron capture event $\tau_{i=r,s}$ compared to the time scale of the beta-decay process τ_{β^-} of the resulting elements. Thus, in the r-process, that usually takes part in harsh environments such as supernovae explosions or collisions of neutron stars, the flux of neutrons is high enough to produce several neutron capture events before a beta decay process takes place, thus $\tau_r \ll \tau_{\beta^-}$. On the other side, the time scale of the s-process is not small enough to produce in most cases more than one neutron capture event before the resulting nuclei decay $\tau_s > \tau_{\beta^-}$, the s-process then generates new elements following the stability valley.

In figure Fig. 4, a detail of the nuclear chart is shown, the green line represents the typical s-process path, the red arrows represent beta decays coming out from elements synthesized far from stability valley as a result of the r-process. Squared elements represent those which can be synthesized by means of just one kind of nucleon-capture process. In this sense, yellow colour represents p-only (proton capture) elements, red squared elements are r-only elements and green coloured are the s-only elements. S-only elements cannot be synthesized by means of r-process as there is a stable element in the same isobar (element with the same mass number A, thus represented by diagonal lines) where the r-process decay chain ends.

⁴ The existence of two different neutron capture processes was concluded following several aspects observed from the isotopic pattern in the nuclei chart as can be the existence of the so-called shielded isobars (see text).

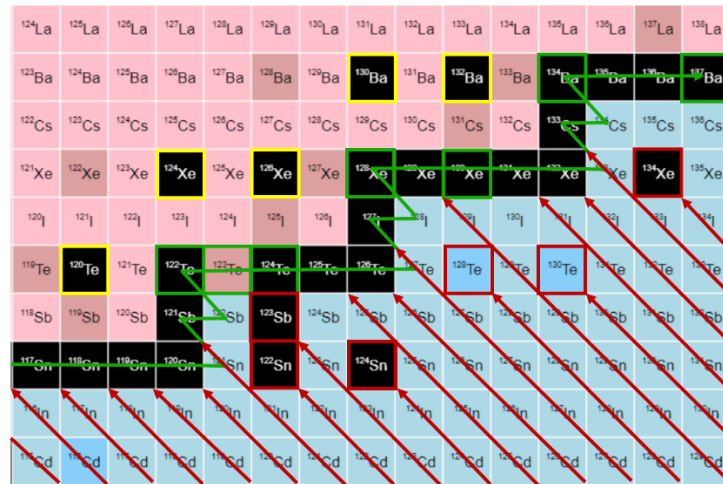


Fig. 4.- Detail of the chart of nuclides with the r-process chain (red line) and the s-process chain (green line) represented. The squared elements are those only accessible by means of just one type of p- (yellow squared), r- (red squared) and s-process chain.

Since the first theory establishing the neutron capture process as a potential way of creating heavy elements [13], substantial progress in stellar evolution models has been achieved based on the following topics [18]:

- Nuclear physics inputs: Including neutron capture cross sections, neutrons source reactions and beta decay half-lives.
- Computational codes: Able to simulate stellar evolution of the stars on the basis of the nuclear physics inputs.
- Astrophysical observations: these can be compared with the predictions coming from computational codes in order to estimate the accuracy of the model used and to determine physical conditions at different stellar evolutionary stages.

In this sense, getting accurate nuclear physics inputs becomes a priority in order to get a realistic and complete description of the s-process. The measurement of neutron capture cross section seems to be one of the most important task as remarked in the B²FH paper where it is emphasized that “unambiguous results would be obtained by measuring the total absorption cross section. It is our view that such measurements would serve as a crucial test of the validity of the s- process”.

For every kind of nuclear reactions, the cross-section (measured in barns $1b = 10^{-28}m^2$) is defined as the effective cross sectional area that a particle presents to any kind of interaction and reflects the probability of a reaction to occur. It turns out that in case of the neutron capture reaction, the cross-section depends mostly on:

- Target’s nature
- Neutron’s energy

As mentioned before, the s-process takes part at a low neutron density of 10^6 up to 10^{11} n/cm³. Regarding neutron’s energy, the most important fact is that neutron’s kinetic energy should be the appropriate to maximize the time that a neutron remains in the vicinity of the nucleus seed, thus the relative velocity between target and neutron should be as less as possible.

Inside of the stellar environment the kinetic energy distribution of the neutron can be related to temperature making use of a Maxwellian distribution.

$$\Phi = \frac{dN}{dE_n} \sim \sqrt{E_n} \exp(-E_n/kT) \quad (2)$$

Where the number of neutrons N shows a dependency with the neutron energy E_n , which depends on k , the Boltzmann constant and the temperature T . Taking this into account, we talk about neutron temperature when referring to its kinetic energy kT . In the case of the neutron-capture reactions, the cross section decreases as the neutron energy grows this can be seen in figure FIG. The most suitable neutron energy to give rise to a neutron-capture is about 0.025eV which is the most probable energy at a temperature of 290 K in the Maxwell-Boltzmann distribution, these neutrons are called thermal neutrons.

On the basis of neutron-capture cross-sections knowledge and the abundances observed, the first classical model of the s-process tried to estimate the rate of change of the abundance of nuclei N_A with mass number A considering that the neutron flux was low enough to almost always decay to a stable isobar before a new neutron-capture event takes part. From this assumption, the rate of change results to be [19]

$$\frac{dN_A}{dt} = -n_n \langle \sigma v \rangle_A N_A + n_n \langle \sigma v \rangle_{A-1} N_{A-1} \quad (3)$$

Where n_n is the neutron number density and $\langle \sigma v \rangle_A$ is the thermally-averaged neutron-capture cross-section for the stable isobar of mass number A . We can write $\langle \sigma v \rangle_A$ as $\sigma_A v_T$ where v_T is the thermal velocity of neutrons and σ_A is the Maxwellian averaged cross section (MACS) that is given in terms of v_T . If we introduce the definition of the neutron-exposure

$$d\tau = n_n v_T dt \quad (4)$$

Then, equation Eq. 3 becomes

$$\frac{dN_A}{d\tau} = -\sigma_A N_A + \sigma_{A-1} N_{A-1} \quad (5)$$

In the case the s-process reaches a steady state, then $\frac{dN_A}{d\tau} \rightarrow 0$ and $\sigma_A N_A \rightarrow \text{constant}$.

In 1965 Seeger et al [20] were able to reproduce the solar distribution of s-nuclei by introducing a neutron-exposure distribution in the form:

$$\rho(\tau) = \frac{f N_{56}}{\tau_0} e^{-\tau/\tau_0} \quad (6)$$

where f is a constant and N_{56} is the initial abundance of ^{56}Fe seed. Later Clayton & Ward [21] found that for an exponential average of flows in the s-process then the next relation is fulfilled:

$$\sigma_A N_A = f N_{56} \tau_0 \prod_{A'=56}^A [1 + (\sigma_{A'} \tau_0)^{-1}]^{-1} \quad (7)$$

Thus, a fit with the data obtained to the empirical $\sigma_A N_A$ for s-only nuclei could give us the information required to know the exposure distribution. The characteristic product of cross-section times s-process abundances for the solar system ($\langle \sigma N \rangle$) is shown in figure Fig. 5, in that picture we can see two important facts.

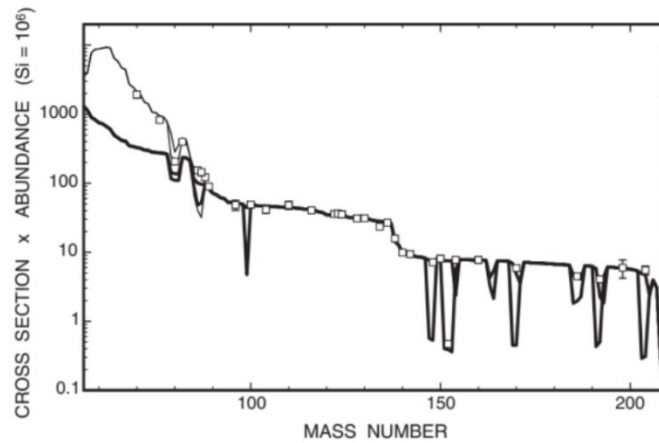


Fig. 5.- Neutron-capture cross-section times s-process abundances in the solar system as a function of the mass number A . The thick line represents the so-called main component meanwhile the thin line represents the sum of the weak and the main component (see text). Dots represents empirical products for the s-only nuclei.

The first aspect is related with the existence of two s-process components: the first, called “main component” (thick line), is the responsible of synthesizing elements with mass numbers $90 \leq A \leq 204$ and it is supposed to take place in low mass stars placed in the Asymptotic Giant Branch or AGB [18] [22]. The second, the thin line, represents the sum of the main and the so-called “weak component” and it is thought to be responsible of producing nuclei with mass number $A < 90$ in the core He- and shell C-burning stages of massive stars.

The second remarkable fact is the existence of the so called branching points, that can be seen as depressions on the FIG distribution. The latter dips, arise as the s-process gets to an unstable element with a beta decay mean life time comparable to that of the neutron capture time scale, thus the element can capture a neutron before decaying or vice versa. In figure Fig. 6 it is shown the ^{79}Se branching point. The measurement of this element is, in fact, one of the main objective of the HYMNS project.

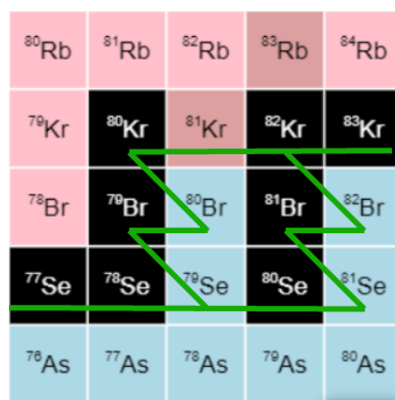


Fig. 6.- Detail of the ^{79}Se branching point. Branching points arises in elements where the neutron capture time scale is similar to the β -decay mean-life time ($\tau_n \sim \tau_\beta$). The probability of the resulting nuclear reaction is given by the branching ratio B .

Neutron-capture cross-section measurements of the elements in the branching points reveal themselves as one of the most important task within stellar evolution calculations. The probability of either a β -decay or neutron-capture reaction take place is given by the branching ratio [18] [22]:

$$B = \frac{\lambda_{\beta}}{\lambda_{\beta} + n\langle\sigma_n\rangle v_T} \quad (8)$$

As usual, $\langle\sigma_n\rangle$ is the neutron-capture Maxwellian Averaged Cross Section of the isotope placed at the branching point (in e.g. ⁷⁹Se in figure Fig. 6), n is the neutron density, v_T is the neutron thermal velocity and λ_{β} is the β -decay rate of the isotope. All these parameters show a dependence on the temperature and can be related to direct observations because branching ratio can be also defined as:

$$B = \frac{\langle\sigma_n\rangle_p N_p}{\langle\sigma_n\rangle_f N_f} \quad (9)$$

where N_p is the isotopic abundance of the heavier stable isotope partially bypassed on the left branch and N_f the isotopic abundance of the fully bypassed isotope (in e.g. ⁸⁰Kr and ⁸²Kr in figure Fig. 6). In summary, we can conclude that physical conditions affecting the parameters present at equation Eq. 8 can be inferred by means of accurate neutron-capture cross-section measurements and astrophysical observations over isotopic abundances.

2.3.- MEASUREMENT OF NEUTRON CAPTURES RATES

Once the importance of neutron capture cross sections in stellar model calculations has been exposed, we will briefly summarized different techniques involved in (n, γ) cross-section measurements along with the facilities used for this purpose. The progress achieved in neutron beam production and gamma-ray detection allowed to determine (n, γ) cross sections with such an accuracy that uncertainties of few percent were achieved in several cases. This progress have included advances in both pulsed neutron sources and radiation detectors.

2.3.1 PULSED NEUTRON SOURCES

There are various methods of generating neutron beams for the study of their interaction with matter including (p,n) [23], (γ ,n) [24] [25] and spallation reactions. Koehler [26] compared the available neutron source facilities in order to estimate the best option for astrophysical experiments and it was concluded that spallation sources are unique because of their peak neutron flux in the keV region, which is the astrophysical relevant energy range. Among the existing spallation facilities, in which e.g. DANCE at LANSCE [27] or NRI at J-PARK [28] are included, CERN n-TOF [7] shows the largest instantaneous neutron flux and has a very long flight-path in EAR1, thus becoming specially well suited for the measurement of small and/or radioactive samples, such as those foreseen within the HYMNS Project.

At CERN n-TOF a 20 GeV/c proton beam with a nominal intensity of 7×10^{12} protons/pulse impinges with a typical rate of 0.4Hz onto a lead spallation target producing on average 300 neutrons per incident proton. A fraction of the neutrons produced travels through a nearly 200 m flight-path until they reach the experimental area EAR1. At this place, a sample enriched with the nuclei of interest is placed centered with the beam. The energy that carries each neutron is directly obtained by measuring the time they need to travel from the spallation point to the

capture sample. This is accomplished by means of flash Analogue-to-Digital-Converter modules, which record every detector pulse, including the arrival of the prompt gamma-flash produced during spallation, which is used as temporal reference. This approach allows one to measure the cross section over a very broad neutron energy range, from thermal (0.025 eV) up to MeV neutron energies, thus enabling the posterior complete determination of the MACS at any stellar thermal energy range from 1 keV up to several hundreds keV.

2.3.2.- NEUTRON CAPTURE DETECTORS

When a neutron capture process is produced, the captured neutron will at first populate an excited energy state and then will decay to the lowest energy state allowed, the energy of the gamma ray cascade emitted is the better information source from which the binding energy of the captured neutron can be inferred. Two main approaches have been developed in order to measure gamma-ray cascade.

A.-Total absorption calorimeters

This kind of detector reaches almost a 100% gamma-ray detection efficiency. Additionally, this detection system typically based on a nearly 4π array of 40 large BaF₂ inorganic crystals [29], shows a rather good energy resolution. The energy resolution, usually measured in terms of Full Width at Half Maximum (FWHM), gives an account of the capability to resolve two different peaks within an energy histogram.

$$Resolution = \frac{FWHM}{E_{Max}} \quad (10)$$

The first calorimeters made use of large liquid scintillators tanks, which were then replaced with BaF₂ crystals because of their superior energy resolution despite of their higher neutron sensitivity. This kind of detector has been and is being extensively used for several determinations of accurate cross sections and MACS values. One example is the complete set of lanthanide isotopes measured with the TAC technique between ¹⁴¹Pr and ¹⁷⁶Lu [18] [30] [31]. These measurements were relevant due to the fact, that the relative s-process abundances of these elements are very well known [32] so that the s-process reaction chain and the associated branching points could be consistently followed. This allowed to confirm the success of the stellar s-process in thermally pulsing low mass AGB stars [33].

B.- Total energy detectors

One of the main drawback found with the use of Total Absorption Calorimeters is the fact that the construction of 4π detectors leads to the use of a large amount of both sensitive and dead material, where scattered neutrons from the sample could be captured⁵. They have a significant neutron sensitivity that, in several important cases may contaminate the measurement and is difficult to correct for.

A new approach on the development of neutron capture detectors was introduced with the first Moxon-Rae detector [1]. The idea behind the development of this detector is based upon two assumptions:

⁵ In some experiments, the percentage of scattered neutrons raised up to 90% of incident neutrons.

- (i) A low efficiency gamma-ray detection system ($\varepsilon_\gamma \ll 1$)
- (ii) Gamma-ray detection efficiency is a linearly increasing function of energy ($\varepsilon_\gamma = kE_\gamma$)

If these two conditions are met by the detection system (originally Moxon-Rae detectors), then, as shown in the equation below, the probability to detect a neutron capture event is well defined and becomes a constant value proportional to the total capture cascade energy. For this reason, this kind of detector is also referred to as Total Energy Detector (TED).

$$\varepsilon_{cascade} = 1 - \prod_{i=1}^m (1 - \varepsilon_\gamma^i) \sim \sum_{i=1}^m \varepsilon_\gamma^i \sim \sum_{i=1}^m kE_\gamma^i = kE_\gamma^{Total} \quad (11)$$

The latter expression ensures that no systematic bias is introduced in the cross-section determination due to the particular capture gamma-ray detected in each event, or nuclear features of the cascade path, which may change from one resonance to another within the same isotope of interest.

The rate of (n,γ) reactions produced can be then obtained just by dividing the total energy estimated E_γ^{Total} by the excitation energy of the bounded nucleus, that is given by:

$$E_{excitation} = E_n \left(\frac{A}{A+1} \right) + E_B^{(n)} \quad (12)$$

where E_n is the incident neutron energy, A is the atomic mass of the target nucleus and $E_B^{(n)}$ is the neutron binding energy.

In order to fulfil the first condition i) and avoid systematic uncertainties, the efficiency of Moxon-Rae detectors had to be small enough so that no more than one gamma ray was detected per cascade. Additionally, it was difficult to obtain a good efficiency-energy proportionality only by hardware means, such as those involved in the Moxon-Rae detectors. For this reason the so-called Pulse-Height Weighting-Technique (PHWT) was developed [2], which allowed for a larger flexibility in terms of the radiation detector itself. This technique allows to ensure the proportionality between deposited energy and gamma-ray efficiency a posteriori by an offline weighting function W_j applied to detector's response R_j^i by defining:

$$\sum_j W_j R_j^i = kE_\gamma^i \quad (13)$$

Nowadays the common approach to obtain the desired weighting function is based on Monte Carlo simulations of the detection system response for a series of gamma-ray energy in the energy range of interest, i.e. from few keV up to the neutron capture energy [4] [34].

3.- THE i-TED CONCEPT

3.1.- STATE-OF-THE-ART AND SCIENTIFIC MOTIVATION

As it has been stated, a better understanding of the s-process and its relation with stellar evolution requires an interdisciplinary approach involving improved nuclear physics inputs, advanced stellar model codes, and a wealth of data from astronomical observations. Referring to (n,γ) cross-sections measurements, although progress made in capture-rates measurement techniques led to more accurate results, essentially the same apparatus (TACs or TEDs) have been used for the last 10-20 years. On the other side, large progress has been achieved in the field of astronomical observations thanks to the development of advanced high-resolution spectrographs [35] [36].

We find ourselves in a situation where uncertainties obtained in meteorite analysis and astronomical observations are smaller than those arising from capture cross-section measurements, and what is more important, several of the most relevant stellar neutron capture rates, mainly for radioactive s-process branching points, still remain unmeasured. If this nuclear data became experimentally accessible, it would be possible to disentangle first-hand-unique-information about the physical conditions in the interior of massive stars and low-mass AGB-stars at specific stages of their evolution.

Nowadays nearly 20 unstable branching nuclei still remain unmeasured [18]. One of the objectives of the HYMNS project is the first measurement of the (n,γ) cross section of ^{79}Se . This rate is of particular interest because of two facts. In one hand, the partially and fully bypassed stable isotopes described in equation Eq. 9 of section Sec.2.2 (^{80}Kr and ^{82}Kr) are known to be s-only type, thus, all the information obtained can be accurately related to s-process contributions. An example of the relevance of such kind of isotopes can be seen on the measurement of ^{151}Sm [37] which served to constrain the temperature during He shell burning in asymptotic giant branch (AGB) stars. On the other hand, the β -decay rate of ^{79}Se shows a well-defined exponential dependence over the thermal region of astrophysical interest, thus, precious information on the thermal conditions in stars, where the isotope is being synthesized, can be derived as stated in section Sec.2.2. Other isotopes don't present this strong thermal dependence as it is the case of the ^{63}Ni measured at CERN n_TOF [38]. The latter represents an important source of information about neutron densities on different stages and layers of evolution of massive stars.

In the aforementioned measurements, as well as for the measurement of the radioactive isotopes representing s-process branching points, one of the main background sources arises from neutrons scattered in the sample that are then captured on the surrounding materials, prompt or after thermalization. This effect has been precisely studied and described in [39], which shows that gamma-rays coming from neutrons captured in the walls of the experimental area represent the main background limitation in the relevant energy range for astrophysics. To a large extent, this has been a constraint in recent (n,γ) experiments, particularly those involving small amounts of radioactive samples [40] [38], a situation which has led to a limited astrophysical interpretation of the corresponding branching nuclei [41].

In this respect, a change of paradigm is expected to come from the development of the so called Total Energy Detector with γ -imaging capability (i-TED). With respect to the state-of-

the-art C₆D₆ TEDs, i-TED will provide additional spatial information about the registered radiation. The latter can be used on an event-by-event basis in order to discriminate contaminant background γ -rays, from true capture γ -rays. Thus, providing a superior level of background rejection. This idea is explained in more detail in the following subsections.

3.2.- i-TED DESCRIPTION

The design of the iTED was made in order to obtain a significant reduction of the background signal coming from neutron capture events produced in both the detector volume and experimental hall materials. The solution proposed is the combination of the Pulse-Height Weighting Technique with a Total Energy Detector for which imaging capabilities are provided.

Imaging capabilities can be introduced in several ways, as for example using gamma-ray cameras featuring a pinhole collimator or a coded-mask collimator [6]. However, such solutions present a very low detection efficiency and a prohibitive intrinsic neutron sensitivity. On the other hand, the electronic Compton collimation technique allows one to enhance detection efficiency, while reducing the amount of structural (dead) materials at the same time. The approach proposed for i-TED consists of exploiting the Compton scattering law by using the so-called Compton modules. These modules consist on a first position sensitive detector (scatter PSD), where the incoming radiation is expected to undergo just one Compton interaction. The remaining energy of the scattered gamma-ray is assumed to be deposited in a second-thick-detection layer (absorber PSD). Both scatter and absorber PSDs were designed to consist of a large continuous scintillation crystal coupled to a pixelated SiPM. In order to obtain a larger and optimized detection efficiency, 4 Compton detection modules would be placed surrounding the radioactive sample. This would allow to the beam-time required for the experiment within reasonable limits.

The proposed i-TED setup is schematically shown in figure Fig. 7, the ⁶LiH layers introduced are absorbers for the neutrons scattered from the sample, following the same methodology as in TAC measurements [7].

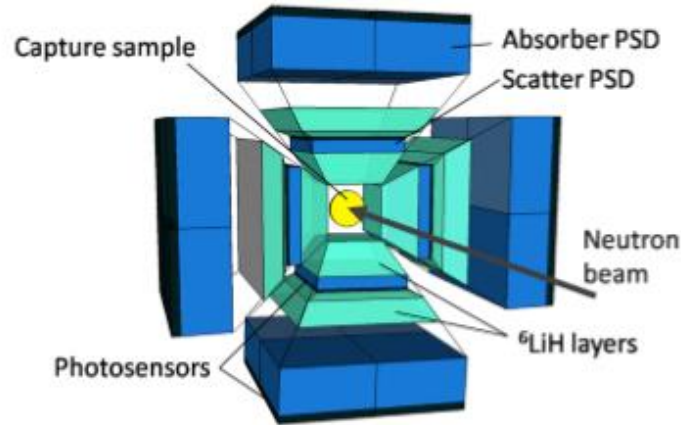


Fig. 7.- Schematic view of the proposed i-TED detection system. The blue cubes coupled to black surfaces represents the position sensitive detectors (PSDs). The ${}^6\text{LiH}$ Layers act as absorbers for the scattered neutrons in the sample (yellow sphere) as used in TAC measurements at CERN n_TOF.

At present, an electronically collimated gamma-ray imager, an i-TED prototype (see figure Fig. 8), is being developed in order to perform first proof-of-principle measurements at CERN n_TOF. Figure Fig. 8 shows a picture of the prototype along with a detail of the software developed in order to control the apparatus working parameters, the readout electronics and to make first on-line analysis of the data being acquired.

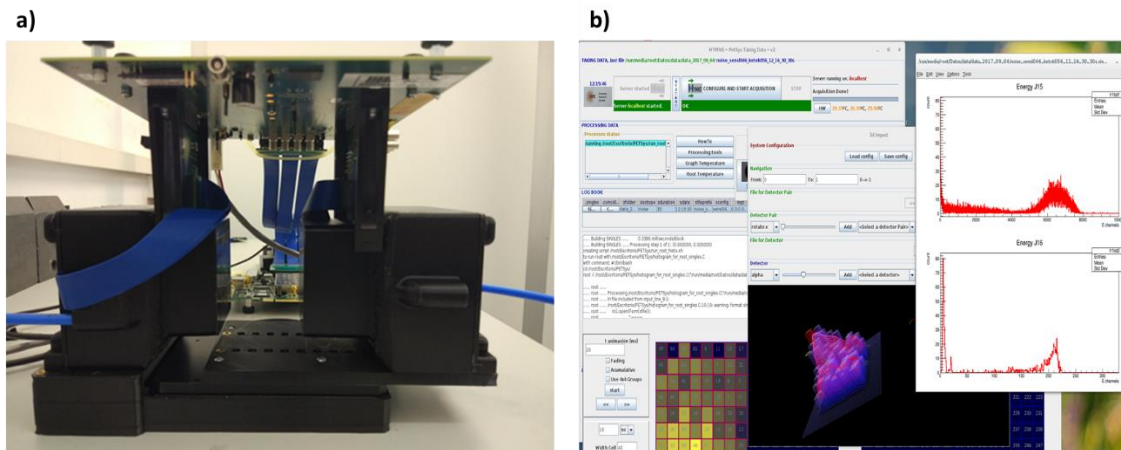


Fig. 8.- a) Picture of the i-TED prototype being developed at the present. The black boxes contain two Position Sensitive Detectors (PSDs) with a 10 mm and 20 mm $\text{LaCl}_3(\text{Ce})$ Crystals coupled to pixelated SiPMs ($6 \times 6 \text{ mm}^2$ pixel size). The readout electronics system can be seen coupled above the PSDs. b) Detail of the software developed in order to manage the i-TED detection system.

3.3.- COMPTON IMAGING

Gamma-ray imaging on the basis of Compton's principle has been shown to be extraordinarily successful in areas like astronomy or medical physics, but before the present HYMNS project it was never proposed or applied in the field of neutron-capture measurements.

Let us suppose an incoming gamma-ray that undergoes a Compton interaction at a measured position r_1 and the scattered gamma-ray is detected at point r_2 as sketched in figure Fig. 9. Measuring both the energy deposited in \vec{r}_1 (E_1) and in \vec{r}_2 (E_2) allows us to determine a cone surface that is susceptible to contain the radiation source of the incoming gamma-ray. Cone's axis is given by normal vector $\frac{\vec{r}_1 - \vec{r}_2}{|\vec{r}_1 - \vec{r}_2|}$ and its amplitude θ is given by the Compton scattering law [42]:

$$\theta = \arccos\left(1 - m_e c^2 \left(\frac{1}{E_2} - \frac{1}{E_2 + E_1}\right)\right) \quad (14)$$

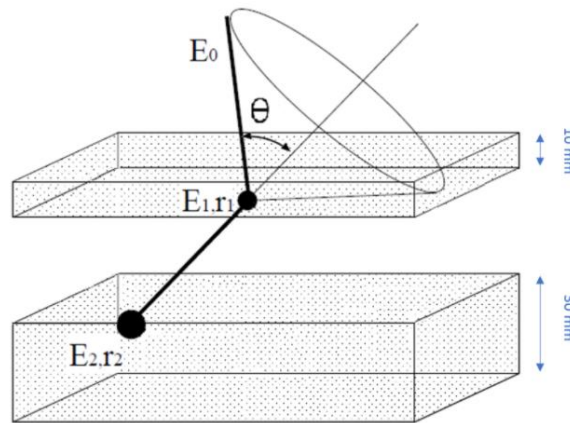


Fig. 9.- Reconstruction of the Compton cone generated by measuring the energy deposited (E_1 and E_2) in two different Position Sensitive Detectors at r_1 and r_2 respectively. The angle θ is given by the Compton scattering law.

In the iTED's Compton modules both, energy deposited (E_1 and E_2) and interaction positions at scatter (r_1) and absorber (r_2) detector are measured in order to reconstruct the Compton's cone on an event-by-event basis. By means of combining this Compton cone information with the known sample position and size, which are well known by set-up construction, it becomes possible to examine whether the Compton cone of each measured gamma-ray overlaps with the sample volume, which would indicate a true capture event in the sample, or if it does not overlap, which would rather reflect a contaminant neutron capture in the walls or elements surrounding the capture sample.

Although as described above, the i-TED methodology itself for (n, γ) measurements does not directly or necessarily involve to reproduce an image of the measured radiation, it is worth mentioning that the implementation of Compton imaging techniques, such as backprojection

methods [43] or origin-ensemble algorithms [44] are planned in order to characterize the overall i-TED system performance in terms of energy- and position-resolution. Indeed, dedicated imaging measurements in the laboratory with punctual gamma-ray sources of different gamma-ray energies, placed at controlled positions are foreseen in order to evaluate and validate the mean performance of the detectors before their implementation for (n,γ) measurements at CERN n_TOF. As it is described below, this kind of technical validation measurements based on gamma-ray imaging are expected to provide valuable information about the average performance of the system, which in turn can be confronted with MC-simulations in order to evaluate the expected system capability to disentangle background from good capture events.

The uncertainties introduced by the spatial and energy resolution of the detectors have been investigated in a recent work within the HYMNS group [45]. These experimental incertitudes give rise to both, an uncertainty in the Compton cone axis and in the angle θ . As a result, the obtained conical surface from the radiation source would be broader than the source itself, thus several ‘unwanted’ background events would be accepted (see figure Fig. 10-a) worsening the signal-to-background ratio with respect to the ideal case.

In case that Compton’s imaging objective were to infer radiation’s source position, the previous issue would be reflected as a reconstructed radiation source less resolved than the real one. Two different studies were carried out consisting in the reconstruction of the radiation source position [45]. The source was a punctual and mono-energetic radiation source, systematically varying in the calculation either the energy or the spatial resolution. Changes in the standard deviation (interpreted here as resolution) of the reconstructed position (Fig. 10-b) would give us a quantitative description of the Compton’s modules imaging performance as a function of the experimental uncertainties.

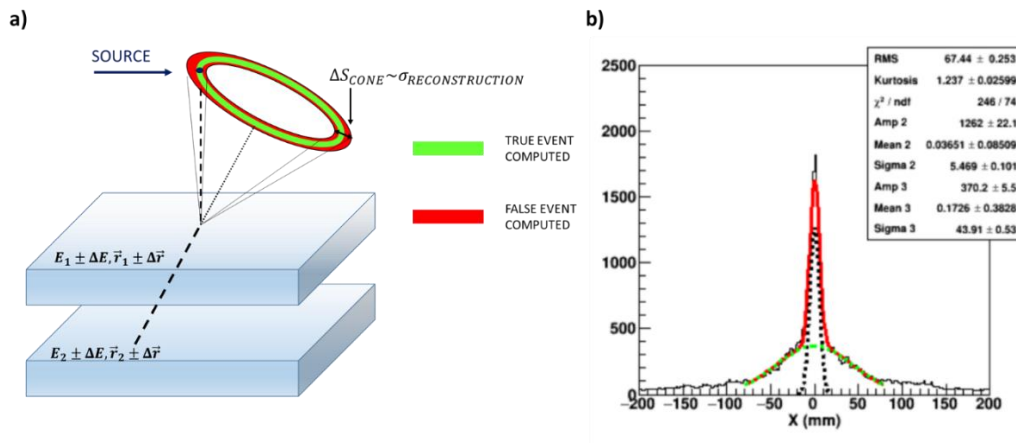


Fig. 10.- a) Detail of the impact of uncertainties in both energy- and spatial-resolution in the Compton-cone surface width. The uncertainty in the position reconstruction is given in terms of the standard deviation of the distribution shown in b), that gives an account of the interaction point reconstruction along the X axis. The spatial distribution can be fitted to two different gaussians represented with red and green lines respectively.

At first, the dependency with energy resolution of the standard deviation for the reconstructed radiation’s source position was obtained considering a constant standard

deviation of 1mm for the X and Y spatial distribution of the gamma-interaction point, and 5mm for the depth of interaction figure Fig. 11-a . In a second study, a constant energy resolution of 3.93% FWHM at 662 keV was assumed (from measurements made in the laboratory), variations in the standard deviation value for the X and Y spatial distribution of the gamma-interaction point were introduced and the resolution of the reconstructed image was measured.

The results obtained can be seen in figure Fig. 11-a and 11-b, and they reveal the relevance of a good spatial and energy resolution in our position sensitive detectors in order to apply accurately Compton's principle for the i-TED imaging capabilities and thus, for background discrimination in (n,γ) measurements. As can be seen in figure Fig. 11-a, fixing the spatial resolution for the reconstruction of the gamma-interaction point, there is an energy resolution (dashed-red line) below which, no better performance is found. On the other hand, for a fixed value of the energy resolution, a smaller value on the X and Y gamma-interaction spatial distribution's standard deviation always leads to a better performance as shown in figure Fig. 11-b. The slope of these two trends also illustrates that efforts in the improvement of the spatial resolution become more valuable, than similar improvements in energy resolution. Indeed, a 1 mm increase of the spatial resolution leads to a loss of 30% in image reconstruction, whereas a change in energy resolution from 5% to 10% has an impact of only about 10% in image resolution.

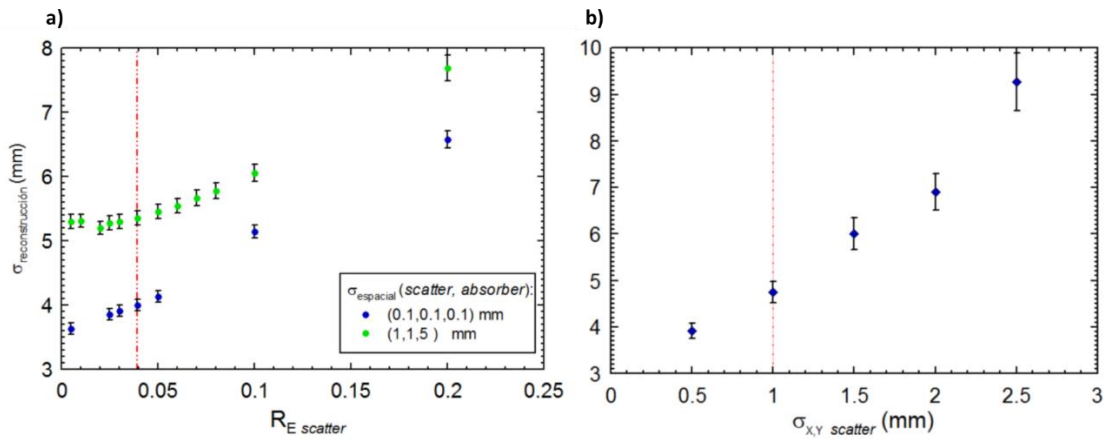


Fig. 11.- Analysis of the impact in the reconstruction of the interaction point (in terms of $\sigma_{reconstruction}$) when varying the uncertainties in a) the energy- and b) spatial-resolution (in terms of $R = \frac{FWHM}{E_\gamma}$ and $\sigma_{X,Y\ scatter}$ respectively) of the position sensitive detectors.

The work summarized above describes the relevance of the two main experimental uncertainties, namely spatial- and energy-resolution. In the present Master-Thesis work, a thorough study of the physics determining those properties is carried out by means of Monte Carlo calculations. The latter are described in the following sections.

4.- ITED POSITION SENSITIVE DETECTORS: PERFORMANCE CHARACTERIZATION AND OPTMIZATION

The main objective of the present work is to study and analyse the energy and spatial response of large monolithic crystals coupled to pixelated SiPM, as they are the basic element of the i-TED detection system, in order to characterise and optimize its performance. The study was made by means of Monte Carlo simulations of large monolithic continuous crystals and ultimately compared with measurements made in the laboratory.

As described in previous sections, the solution followed in order to develop a position sensitive detector with low neutron sensitivity was coupling large continuous monolithic $\text{LaCl}_3(\text{Ce})$ crystals to pixelated SiPM. With such kind of photosensors, the distribution of scintillation photons on the detecting surface can be obtained, which is intimately related to the gamma-ray interaction point within the sensitive volume. In this sense, a smaller size and a larger number of pixels conforming the photosensor should give us a more precise information about the photons distribution itself, and consequently a better spatial response in order to reconstruct the gamma-ray interaction point. However, since a dead region where photons cannot be detected between pixels exists which cannot be reduced, this large number of pixels implies a loss of detected photons and thus, a loss in energy resolution. Therefore, the best compromise between energy and spatial resolutions needs to be found.

In the following subsections a description of the methodology followed during the development of this work is exposed. We will first describe the experimental apparatus used to carry out reference measurements, along with a detailed description of the simulation code implementation. An explanation of the aspects taken into account in order to implement algorithms used to obtain the desired interaction point reconstruction will be exposed.

4.1.- EXPERIMENTAL APPARATUS AND METHODOLOGY

4.1.2- Scintillation crystals

The use of inorganic scintillation crystals as radiation detectors are based on their electronic properties, more specifically, their electronic structure band. An electron placed in the valence band can be excited due to ionizing radiation, and it can then be placed in either the conduction band or the exciton band, creating a hole in the valence band that can be filled with a de-excited electron with the subsequent scintillation light emission. Impurities are added to the material to modify the electronic structure band in order to obtain scintillation photons with wavelengths in a certain range.

The most relevant features that determine the performance of scintillation crystals are:

- Emission spectra: since scintillation photons are emitted over a wide range in wavelength which, as electromagnetic waves, can be absorbed by the crystal, the

scintillation crystal must have an emission spectra defined over a different range than the absorption spectra in order to become transparent to its emitted light.

- Scintillation yield: the number of photons generated per energy deposited.
- Linearity: scintillation yield should be linearly proportional to energy over the wider range possible.
- Fast time response: scintillation light is emitted in different time scales as is produced by different processes as prompt fluorescence (fast component) and phosphorescence (slow component). Scintillation crystal should convert the larger fraction as possible of the incident radiation energy to enhance prompt fluorescence, thus ensuring a fast time response.
- Another important aspect in the election of a scintillator is its refractive index, that should be as close as possible to the material acting as a waveguide for the emitted light to avoid light loss.

In the design of the Compton imaging system, inorganic crystals of LaBr₃(Ce) or LaCl₃(Ce) were proposed due to their high energy resolution, fast timing response, good linearity, and high light output. In the first i-TED prototype LaCl₃(Ce) crystals were used as they present a lower neutron sensitivity.

We have performed characterization measurements with three different LaCl₃(Ce) crystals (figure Fig. 12) with a square size of 50x50 mm² and thicknesses of 10 mm, 20 mm and 30 mm, manufactured by Beijing Scitlion Technology Corp [46]. LaCl₃ crystals are doped with Cerium (with a concentration of less than 10%) in order to increase light output and reduce decay time [47]. These crystals have the advantages of presenting a superior energy resolution (manufacturer's nominal values: 4.2% - 5.1%), a fast scintillation decay (28ns presenting a very small percentage of photons emitted in the slow decay time component), excellent linearity response and stability with temperature, and high count rate capabilities.

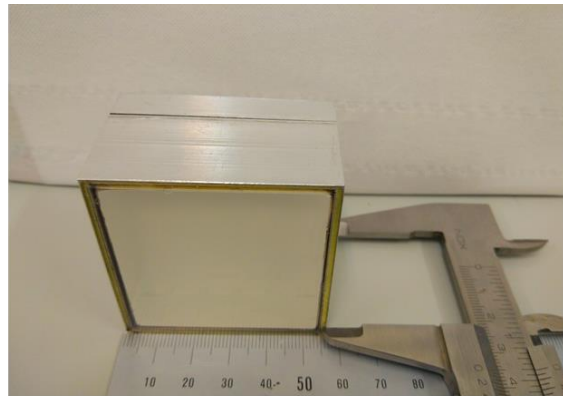


Fig. 12.- LaCl₃(Ce) crystal (dimensions 50 x 50 x 20 mm³) used In the measurements performed for the spectroscopic characterization of the Position Sensitive Detectors designed to form the i-TED detection system.

4.1.2- Photosensors

Photosensors are devices which transform the scintillation light produced in crystals into an electric current that can be measured. In this work, two types of photosensors were used: a

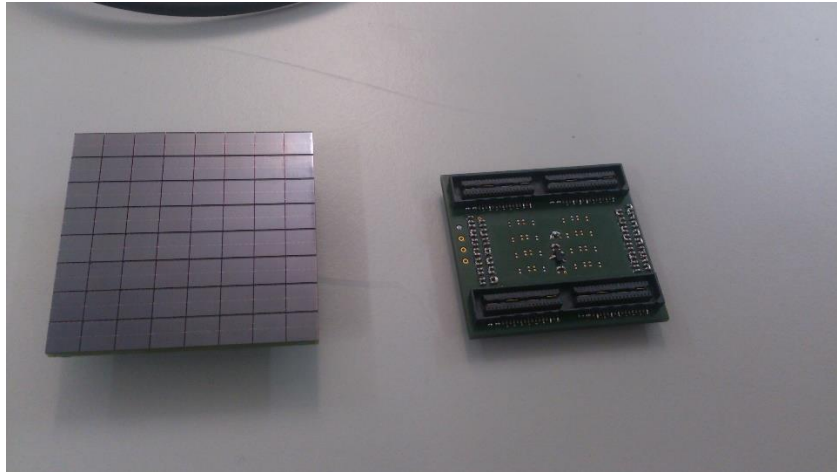


Fig. 14.- Sensel Silicon PhotoMultiplier with an 8x8 pixilation and 6x6 mm² pixel size used to evaluate the loss in energy due to the introduction of dead zones between pixels. The PCB shown is the ASIC based frontout electronics used to couple to the frontend electronics.

4.1.3- Power and readout electronics

A.- PMT Assembly

A Tennelec TC954 high-voltage module was used to power the Hamamatsu PMT at its nominal value of -580 V. The current signal from the last PMT dynode was fed into a Canberra-2005 preamplifier and shaped by means of a Tennelec TC-244 amplifier. The output from the latter was used to obtain the pulse-height spectra by means of a multi-channel analyzer (Palmtop MCA8k-01), which were later analyzed to derive the energy resolution. The exposed apparatus used for measurements with the PMT can be seen in Fig. 14.

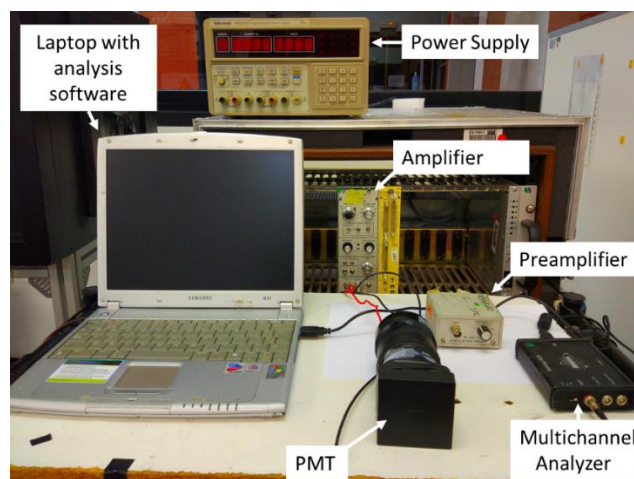


Fig. 14.- Experimental set-up used for to perform the spectroscopic measurements with the Photomultiplier Tube.

B.- SiPM assembly

The SiPM was plugged into a breakout sum-board (ArrayX-BOB6-64S) provided also by the same manufacturer. Such a PCB is designed to merge all the fast-output signals from the SiPM and thus provides a charge-signal proportional to the total number of scintillation photons detected with the SiPM. The SiPM was biased at 5 V beyond the nominal breakdown voltage of 25 V by using a GRELCO GVD305SF voltage-supply unit. The sum of all the SiPM fast-signals was then dc-decoupled by means of a 10 nF capacitor and fed to the Tennelec TC-244 amplifier. The shaped output signal was fed into the MCA for getting the corresponding pulse-height spectrum.

In order to inspect the spatial response of the SiPMs, measurements were carried out also with the PETSys system [48]. The ASIC provided, namely TOFPET2 [49], works as a readout and digitization system being able to manage up to 64 independent channels. In each channel the signal coming out from each pixel is divided and the information contained in the amplitude of the pulse-shape can be inferred either by using a charge integrator ADC (QDC) [50] or using the time-over-threshold (TOT) technique [51]. The performance showed by this system and its scalability makes PETSys the most suitable readout electronics to be used in the development of i-TED. The TOFPET2 ASIC described can be seen in figure Fig. 15.

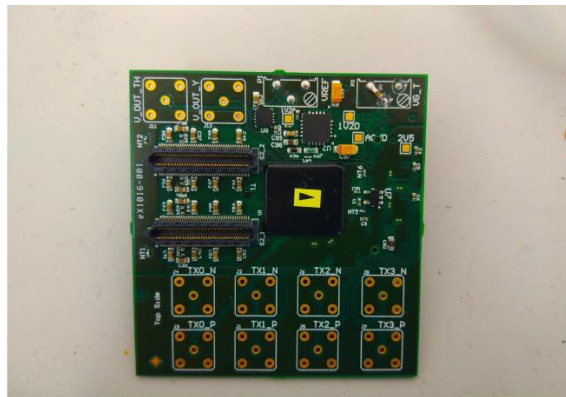


Fig. 15.- ASIC TOFPET2 from PETSys manufacturer, used to perform measurements in order to analyse the spatial response of the Position Sensitive Detectors.

4.2.- SPECTROSCOPIC PERFORMANCE. MEASUREMENTS

Each combination crystal-PMT and crystal-SiPM was calibrated in energy by means of dedicated ^{22}Na , ^{137}Cs and ^{60}Co measurements covering the energy range from 511 keV up to 1332 keV. Additionally, a background measurement was performed in order to subtract the ambient and the intrinsic crystal (α -) background contributions from the source spectrum.

The energy calibrated pulse-height spectra for the three $\text{LaCl}_3(\text{Ce})$ crystals are shown in figure Fig. 16 for both PMT and SiPM readouts. Generally, a rather similar energy response is found for both the SiPM and the PMT. Gamma-ray events leading to full-energy deposition show, in both cases, a very similar signature. The main difference arises in the energy range between the upper Compton edge and the full-energy events, where a higher contribution is found for all measurements made with the SiPM.

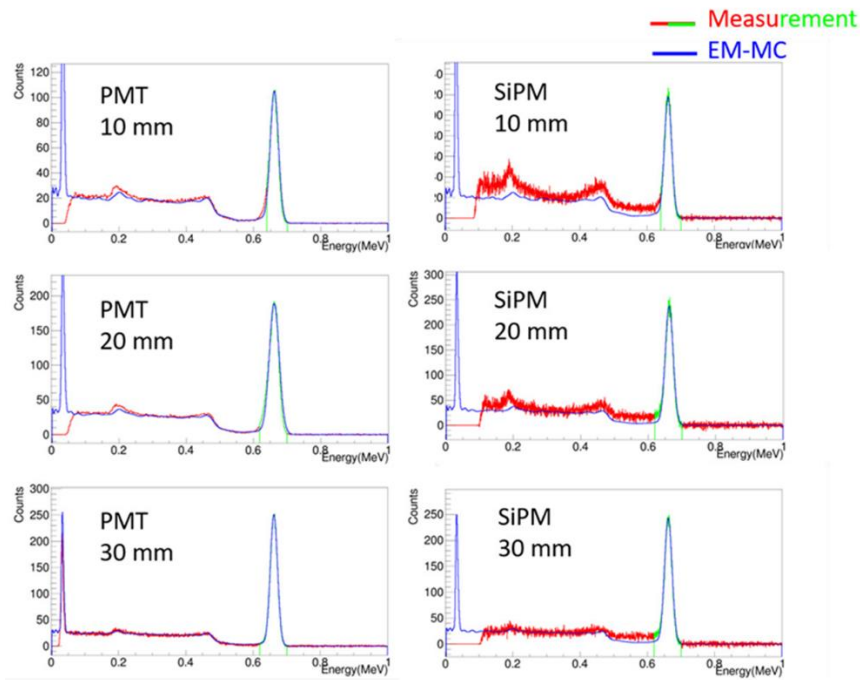


Fig. 16.- Calibrated energy spectra for the ^{137}Cs -source measured with the $\text{LaCl}_3(\text{Ce})$ crystals coupled to the PMT (left column) and to the SiPM (right column). From top to bottom the crystal thicknesses are of 10mm, 20 mm and 30mm.

In order to accurately determine the energy resolution for each crystal-photosensor assembly we have implemented an algorithm, which performs a least-squares minimization between the experimentally calibrated spectrum and the one calculated from electromagnetic interactions of the ^{137}Cs beta-decay using Geant4. The simulated spectrum, initially with an ideally narrow resolution from the MC calculation, is convoluted during the minimization process with a Gaussian distribution until it matches nearly perfectly the measured one (see figure Fig. 16). Hereby, the energy dependency of the Gaussian width is assumed to have a linear dependency with the square-root value of the deposited energy [52]. We have found this approach to be more reliable and substantially more accurate than the commonly used method of fitting a Gaussian function to the experimental spectrum. The results thus obtained for the resolution at 662 keV in FWHM are listed in table TAB and displayed below in Fig. 17.

10 mm		20 mm		30 mm	
PMT	SiPM	PMT	SiPM	PMT	SiPM
4.548(16)%	3.923(7)%	5.254(13)%	4.467(3)%	3.849(3)%	3.936(4)%

Table 1. Energy Resolutions (FWHM) at 662 keV obtained for the three different crystals coupled to the PMT and to the SiPM

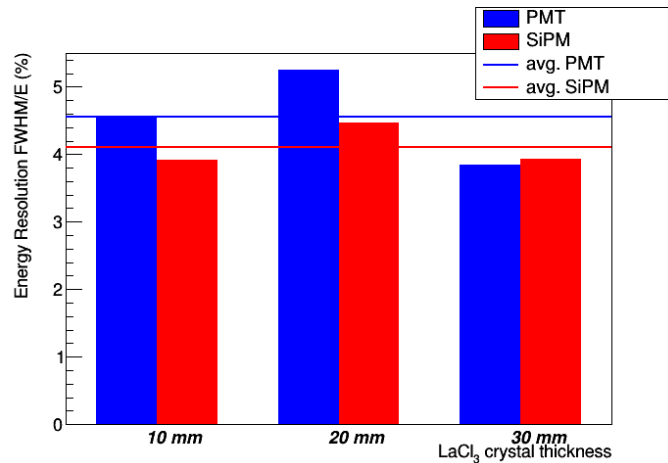


Fig. 17.- Energy resolution (FWHM) at 662 keV obtained for the three different crystals coupled to the PMT (blue) and SiPM (red). Solid lines represent their average values.

The first remarkable aspect is the fact that, the SiPM photosensor yields on average, and for this particular set-up, a better energy resolution than the conventional monocation PMT. On average, the resolution obtained with SiPM readout is of 4.11% FWHM, to be compared with the 4.55% FWHM for the PMT. Variations of about 0.8% and 0.4% are found for individual crystal-photosensor configurations with respect to the average resolution value for PMT and SiPM, respectively (see Fig. 17). This result, which is at variance with the comparison reported in [8] for PMT and SiPM sensors, may well be ascribed, as anticipated in the mentioned article, to the higher quantum photo-detection efficiency and fill factor of the new generation of SiPMs. This aspect will be further discussed in the section below on the basis of detailed MC simulations that include the optical transport and absorption of scintillation photons in the scintillation crystal. Apart from the differences in the average values for the energy resolution, no clear systematic trend has been found regarding the thickness/size aspect-ratio of the crystals.

Two conclusions can be derived from these measurements, which are important for the future development of i-TED. Firstly, LaCl₃ crystals, which are preferred in our case for the lower neutron cross section of Chlorine compared to Bromine [5], can yield an energy resolution, which is comparable to that of LaBr₃ scintillators [8] [9]. Secondly, the performance in energy resolution does not deteriorate when replacing a mono-cathode PMT by pixelated SiPM, on the contrary, it improves in relative terms by about 8%.

4.3.- MONTECARLO SIMULATIONS

Montecarlo simulations have revealed themselves as a powerful tool to perform thorough and detailed studies on many physics fields. Particularly, Geant4 [53] has erected as the most widely accepted simulation toolkit in the field of nuclear and particle physics. Developed over the last 20 years, Geant4 is the result of the effort made by many scientists at CERN in order to achieve a detailed description of the physical processes that take part in the experiments performed.

4.3.1.- GEANT4

We have used the latest version (10.3) of the Geant4 software in order to model our experimental set-up and, in particular, to develop a toolkit which allows us to study the impact of the SiPM pixel size on both the spatial- and energy-response of our system. This will allow us to optimize the design of the i-TED system for optimal energy- and position-response. Furthermore, once we have validated our code by means of the measurements presented in the section above, we use it to explore different aspects related to the spatial sensitivity of our detectors, such as the position reconstruction in the transversal XY plane of the crystal, and the DOI.

Geant4 simulation toolkit is a collection of libraries written in C++ programming language that serves as an easy way to describe an experiment with such a great detail level. To do so, user needs to create a set of C++ files containing all the methods and classes needed to define the experiment description and the simulation dynamics.

A.- SIMULATION DESCRIPTION

The code implemented to perform a simulation in Geant4 is divided in different files that will be loaded and executed by the Geant4 manager class. For each simulation, Geant requires at least the definition of three mandatory classes that are used to build up the simulation. The latter are listed below

- In PhysicsList.cc the physical processes that take part in the experiment must be defined. In our particular case, we have included the electromagnetic processes that affect gamma-ray interactions and the optical processes that affect to scintillation photons.
- The primary particles that are considered to give rise to the chain of events in the experiment, the way they are produced and launched must be defined in PrimaryGeneratorAction.cc. Here, we have defined gamma-rays as primary particles being created by means of either an isotropic ¹³⁷Cs source or collimated pencil-beam of gamma-rays with an energy of 662 keV and 511 keV.
- The geometrical description and material properties of our detector is defined in DetectorConstruction.cc. To this aim we have defined our position sensitive detector to be formed of a LaCl₃ scintillation crystal with a Teflon (PTFE) wrap covering the front and lateral faces. A 10 μm air gap was introduced between the crystal and the wrap. Both the crystal and the wrap are then embedded into an aluminium capsule with a quartz window at the bottom face of the detector, which acts as a wave-guide for the scintillation photons. Since the detecting surface representing the photosensor has been modeled as a continuous surface we can introduce later, by means of an offline analysis, the features of the different photosensors we want to analyze. In figure Fig. 18-a,-b we show a scheme of the PSD along with an event simulated within.

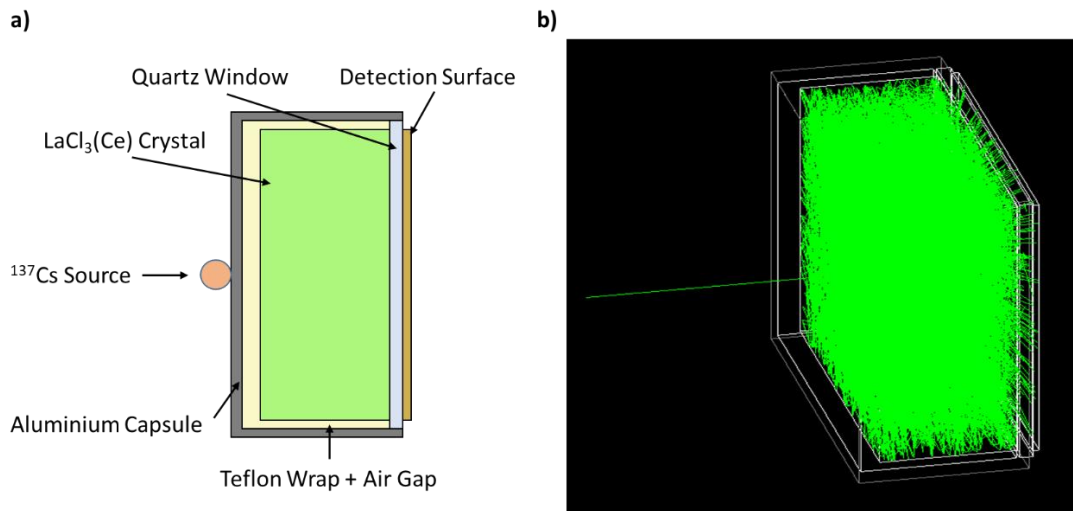


Fig. 18.- a) Scheme of the implemented detector geometry in the simulation with all the materials described. b) Simulation of a pincel-beam impinging if the center of the crystal, when the energy is deposited, several scintillation photons are generated and simulated.

Besides the definition of the mandatory classes, user must define the methods that allows one to control every aspect during the simulation execution. These methods, known as user action methods, are defined in three different files as they will take action at three different levels:

- RunAction.cc contains the actions that should be done at the beginning and the end of the simulation. In our case, we initialize the output file where the data generated is going to be stored and define all the information that we are interested to obtain making use of an analysis manger implemented in Geant4. In this sense, for the whole life-time of a gamma-ray in the simulation we save the number of interactions which the gamma-ray undergoes within the sensitive volume, the total energy deposited in the sensitive volume, the number of scintillation photons produced and the number of scintillation photons detected in the photosensor. Every time a gamma-ray interacts we store the spatial and temporal coordinates of the interaction, the energy deposited and the kind of process giving rise to that interaction. For each scintillation photon that reaches to the detecting surface we also store its spatial and temporal coordinates and its energy, which can be related to its wavelength. To store all this information, three classes were defined namely Event class (Event.cc), Gamma class (Gamma.cc) and Photon class (Photon.cc). At the end of the run, all the structures created are deleted in order to optimize the computational code and the output file is closed.
- After the methods defined to act at the beginning of the simulation are executed, the simulation of the primary particles described in the mentioned PrimaryGeneratorAction.cc starts. These particles are launched one by one and they are treated as singular events. In EventAction.cc we describe what should be done at the beginning and ending of each of these particles simulation. Our aim in this situation is to save all the information obtained by the end of the event. For each event, several entries of gamma interactions and photon detected are stored in arrays and a method to create each new entry of the array is given. At the beginning of the event, the auxiliary variables and arrays used to store the information are cleared in order to avoid data overloading.

- Each event in Geant4 is treated as a series of steps representing different processes. At the beginning of the step, Geant4 takes into account the included physics processes that are susceptible of take part in the step. Then, using Monte Carlo methods decides what is going to happen to the particle until a new process (step) arises. In SteppingAction.cc we analyze the process giving rise to the new step and decide the actions that must be performed. More specifically, we evaluate whether the particle simulated is a gamma-ray or an optical photon, the kind of process simulated, and the volume where the particle is situated. In case we have a gamma-ray interacting in the sensitive volume or an optical photon that reaches the detecting surface, we call to the special method in EventAction.cc in order to create a new entry in the array containing the interesting information.

Besides the implementation of the exposed classes and methods, we must create the main file where the run manager is called and executed, this run manager then calls all the exposed classes and methods. Finally, in order to generate an output file that can be handled by our analysis software, another file called AnalysisManager.cc was created. All the code implemented in the files exposed in this section can be seen in appendix (Appendix A)

B.- OPTICAL PHYSICS

As the photosensor is able to detect scintillation photons, and its distribution over detecting surface is crucial for reconstructing gamma-interaction points, optical physics processes were implemented [54]. The use of the optical capabilities in Geant4 requires, in addition to the optical physics module, the accurate definition of the optical properties for all materials and interfaces involved in the simulation which are included in the detector description. All these properties have been included in our calculation as a function of the photon momentum, covering the wavelength range from 300 nm up to 600 nm, with a binning resolution of 3 nm (see figure Fig. 19).

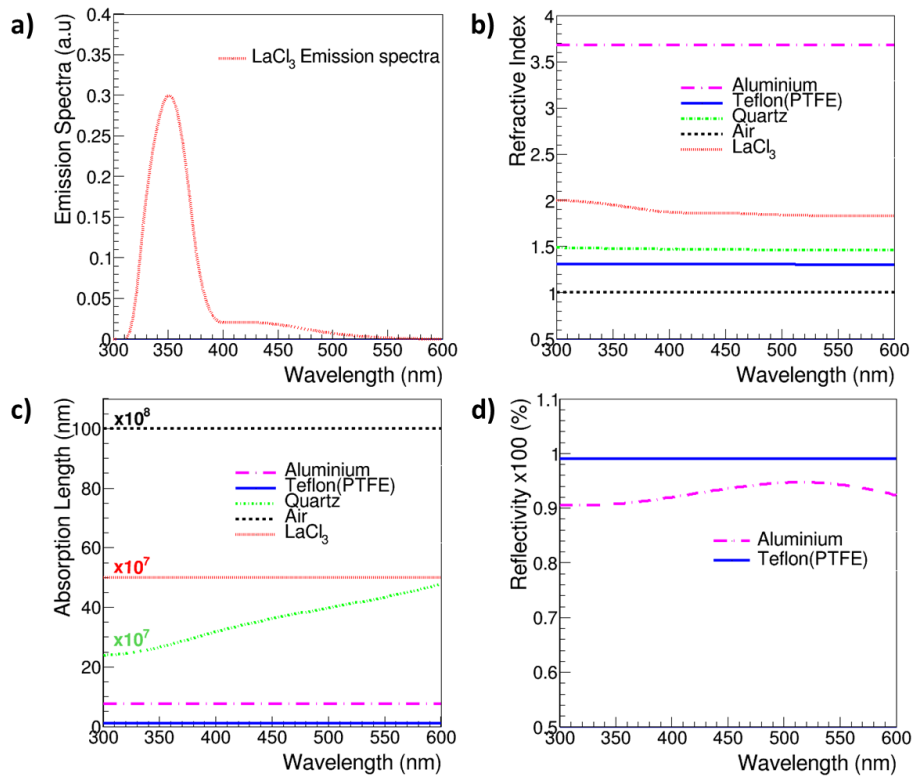


Fig. 19.- Numerical distributions of the main optical properties as implemented in the simulation. Scintillation light distribution for LaCl₃(C3) (a), refractive index for several materials (b), absorption lengths (c) and reflectivity of aluminium and teflon (d).

For the sensitive volume a scintillation yield is provided (Fig.19-a), which accounts for the number of photons produced by the ionizing radiation per keV of deposited energy. The scintillation spectrum is included as a function of the photon wavelength (λ), which was provided by the crystal manufacturer. The definition of the scintillation process involves also the decay time within the fast scintillation component, the yield-ratio or portion of photons emitted via the fast component, and a fudge factor called resolution-scale, which affects the statistical distribution of generated photons. Materials involved in the optical processes are characterized by their refractive index (Fig.19-b), absorption length (Fig.19-c) and, for reflecting materials, reflectivity (Fig.19-d). Although implemented in further offline analysis, we also expose in figure Fig. 20 the implemented quantum efficiency dependence for both PMT and SiPM photosensor.

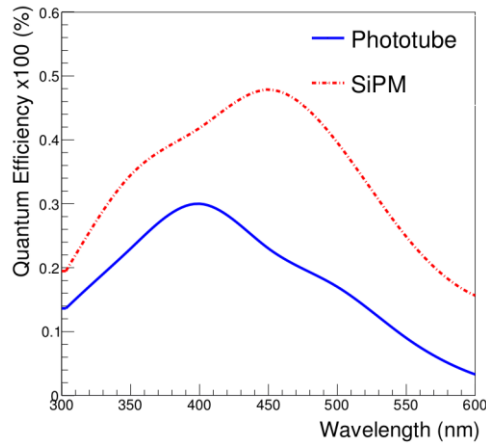


Fig. 20.- Quantum efficiency for the two photosensors used in this study, as provided by the manufacturer and implemented in the code.

Two different approaches are available in Geant4 in order to model the reflection and refraction processes of the scintillation quanta. The *glisur* model applies directly the law of Snell for an incoming photon impinging on a surface. In this case, a rough surface is considered to be a collection of *microfacets* whose normal vectors are the combination of the normal vector for the average surface and a vector obtained with a random point contained in a sphere of certain radius. The latter is given by a free parameter, which is related to the polish-level of the crystal (see Ref [55] for more details). Alternatively, the *unified* model distributes the micro-facets orientation following a Gaussian distribution and photons will undergo a specular reflection in this surface together with other contributions such as backscattering, lobe reflection and Lambertian reflection. The unified model requires a surface characterization and a detailed knowledge of the mentioned contribution probabilities [56], which were not available for the present work. For this reason we used the *glisur* model in our simulations. As it is demonstrated in further sections, the *glisur* model was indeed found sufficiently accurate for a fair reproduction of the measured spectroscopic response. Using this model one can account for surfaces with ground-finish, which lead to a perfect diffuse Lambertian reflector, for surfaces with polished finish, which yield specular reflection, or for a linear combination of them both. The LaCl₃ scintillation crystals used in this work had a polished surface on the side with the optical window, and a rough finish on the other five surfaces (base and walls). However, the degree of roughness was not available and, for this reason, we adjusted the polish-level within the *glisur* model in order to account for this unspecified property. We found a polish level of 0.8 convenient for a reasonable reproduction of our measured spectra, thus indicating a rather specular than diffusive situation. Other features that must be established for the surface definition is the kind of transition between materials, which can be defined as a *dielectric_dielectric* transition or *dielectric_metal*, being the latter the one chosen to define reflecting surfaces. In order to properly account for boundary processes the surface finish needs to be properly defined. In the present version of the code one can choose between *polished*, *polishedfrontpainted*, *polishedbackpainted*, *ground*, *groundfrontpainted* and *groundbackpainted*.

C.- MULTITHREAD MODE

Finally, we have made advantage of the possibility of using the Geant4 multi-thread mode in combination with a multi-core computer. This allows us to execute in parallel separate Geant4 threads concurrently by separate hardware threads, thus enhancing remarkably the processing capability and keeping the total amount of CPU-time within reasonable limits. The efficiency of the parallelization approach is demonstrated in Fig. 21, which displays the results from a series of MC computations covering the range from 1×10^6 up to 3×10^8 scintillation photons, and employing in each MC run 1, 2, 4 and 8 threads. From Fig.21-b, which shows the average CPU time needed for each simulated optical photon as a function of the number of parallel threads, it can be concluded that, increasing the number of threads beyond 8 does not contribute to a substantial reduction of CPU time. For this reason, we carried out all the MC calculations presented below for 8 threads using an intel i7 computer.

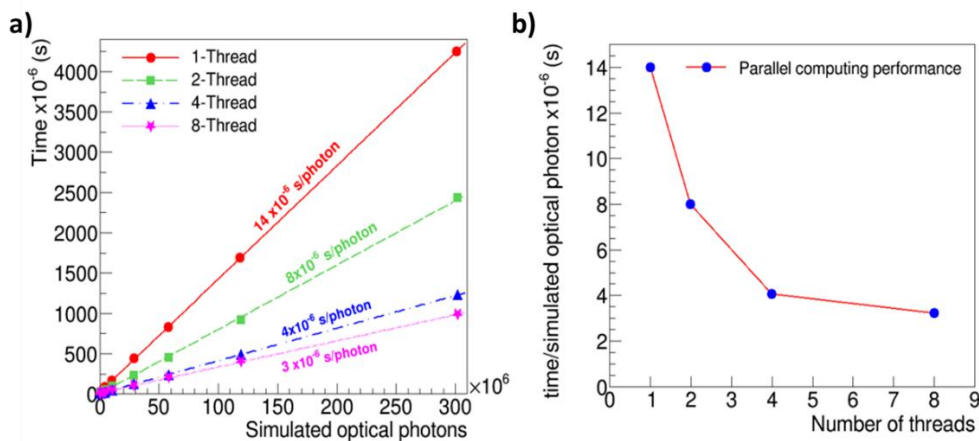


Fig. 21.- a) CPU computation time (s) as a function of the number of simulated optical photons. b) Average CPU time required for each optical photon, as a function of the number of threads.

4.3.2.- ROOT

The analysis of the results coming out from Geant4 simulations was made with ROOT Data Analysis Framework version 6.09/02 [57]. ROOT is a C++ based⁶ Data Analysis Toolkit developed over the last decades at CERN, its high performance is mostly due to the complete data structures integrated which allows a fast data processing and an accurate storage performance that features a high compression rate. Besides this, it is possible to execute easily analysis scripts in order to manipulate the information stored. In the development of the present study we have made use of two different data structures, these are the trees and the histograms, the former provides a flexible way to organize the information obtained, while the latter is a fast and powerful visualization tool.

At first, the stored information coming out from the simulation is not relate, this is, neither gamma interactions nor photons detected are linked to the same event. Linking this information to the same event give us a flexible way to further analysis as, i.e., is it possible to

⁶ It can also be exploited with other languages such as Python and R.

select all the information of the photons or gamma-interactions coming from a certain event that fulfils certain conditions. A first script was implemented in order to organize and relate all the information for the same event. For each event we stored an event ID, the number of electromagnetic interactions of the gamma-ray within the sensitive volume, the number of scintillation photons generated and the number of scintillation photons detected, besides this, each event has linked two arrays, one containing the time/space coordinates and energy deposited for each gamma-interactions, and another array containing space/time coordinates of the detected photons along with their energy.

5.- RESULTS

An appropriate simulation code allows one to study and analyse the impact on the energy and spatial response of the PSD depending on the photosensor modelled. Validation of the code was made by comparing the spectroscopic response measured and exposed in section (SEC), with the results obtained from MC simulations. In this section we will expose the results obtained in order to validate the code and we will introduce the analysis done in order to study both energy and spatial response when using a SiPM photosensors with pixilation sizes of 6 mm and 3 mm.

5.1.- CODE VALIDATION

In order to have a direct comparison between the number of photons detected in the photosensor (as predicted by the simulation) and the measured spectra, the simulation has been scaled on the horizontal axis to translate the calculated photon-number into calibrated energy-units. As demonstrated in figure Fig. 22, the optical simulation of the response function yields a fairly good agreement with the measured spectra, both for PMT and SiPM. With the aim of accurately determining the energy resolution derived from the optical simulation we apply the same convolution algorithm as the one described in section 4.2. For each crystal-photosensor assembly, the ideal electromagnetic MC response is convoluted with a Gaussian distribution until it fits the new optical MC response. Results obtained are listed in table 2 and shown in figure Fig. 22.

10 mm		20 mm		30 mm	
PMT	SiPM	PMT	SiPM	PMT	SiPM
4.779(18)%	4.43(13)%	5.483(10)%	5.181(8)%	3.781(7)%	3.342(3)%
5.06%	12.94%	4.36%	15.98%	-1.76%	-15.11%

Table 2. Energy Resolutions (FWHM) at 662 keV estimated by means of Monte Carlo simulations for the three different crystals coupled to the PMT and to the 6x6 mm² pixelated SiPM. In the last row, the difference in relative terms between the estimated resolution and the measured one is listed.

The results displayed in Fig. 22 indicate a better agreement between simulation and measurements for the PMT with respect to the SiPM. In the former case the largest deviation (5% in relative terms) is found for the 10 mm thick crystal. Regarding the SiPM, differences between the simulation of optical-photons and the spectroscopic measurements are larger for 10 mm and 30 mm thick crystals, with discrepancies of +15.98% and -15.11%, respectively.

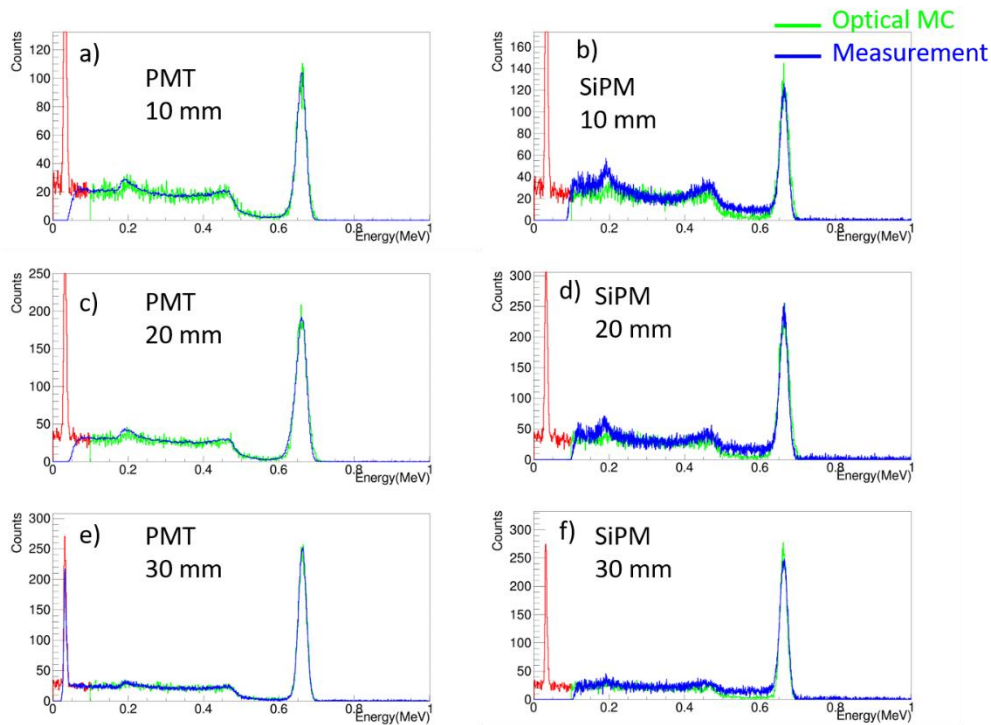


Fig. 22.- Optical MC simulation of the response function (red-green spectra) for the PMT readout (left column) and SiPM (right column). From top-to-bottom the panels show the results for detectors with crystal thickness of 10mm, 20mm and 30mm.

On average, the optical MC simulation for the energy resolution of detectors with SiPM readout (4.31% FWHM) slightly overestimates by 4.8% the average of the measured values (4.11% FWHM). On the other hand, the average value calculated for the crystals assembled to the PMT (4.68% FWHM) are overestimated by only 2.9%. Comparing the experimentally determined average resolution for PMT (4.55% FWHM) versus SiPM (4.11% FWHM), one can conclude that the difference found experimentally (9.7% better resolution for the SiPM), is also fairly well reproduced by our optical MC simulation of the scintillation photons (8.6%).

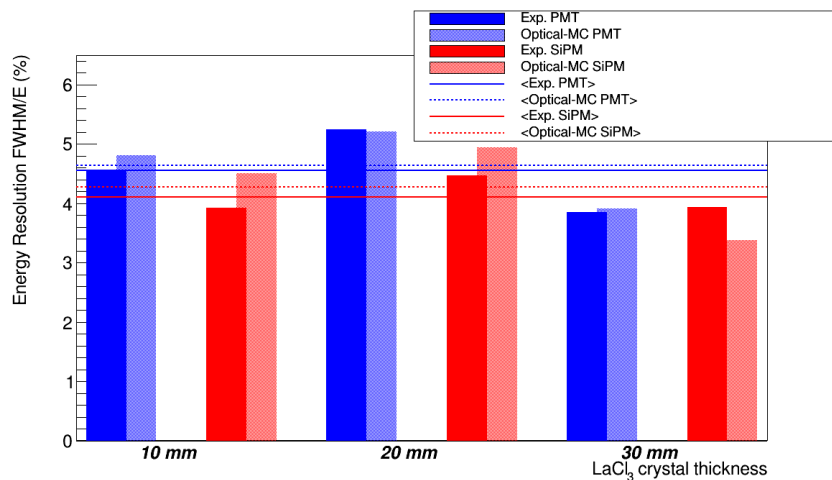


Fig. 23.- Comparison of experimental energy resolution (bold) versus optical MC simulated values (light).

In summary, our simulation toolkit allows us to estimate within 4% (2%) the average energy resolution for large monolithic LaCl_3 crystals optically coupled to pixelated SiPM (PMT). Encouraged by this result, we used our simulation toolkit in order to infer the expected performance of a SiPM with a thinner pixel-size of $3 \times 3 \text{ mm}^2$. For this calculation we used realistic technical values from commercially available SiPM, in particular those from the sensL ArrayJ-30035-64P-PCB. The idea behind this simulation resides on the fact that, although less scintillation photons will be registered due to increasing dead-areas, an enhancement in position reconstruction might be obtained, either on XY and/or XY and DOI, thanks to the thinner sampling resolution.

5.2.- ENERGY RESPONSE

The energy resolution found here for the $3 \times 3 \text{ mm}^2$ pixels is displayed below in Fig.24 and listed in table 3, together with simulated response functions. For determining the energy resolution, we followed the same methodology as above. The ideal response function simulated by means of the EM-MC calculation was convoluted with a Gaussian distribution with a square root dependency on the energy, and the response function from the optical MC simulation was converted to energy units by means of a linear relationship. Thus, the accurate value for the energy resolution of the optical simulation is found for the best agreement between both simulations, as listed in table TAB and shown in figure FIG.

10 mm	20 mm	30 mm
4.595(17)%	4.957(10)%	3.595(5)%
3.71%	-4.32%	7.6%

Table 3. Energy Resolutions (FWHM) at 662 keV estimated by means of Monte Carlo simulations for the three different crystals coupled to the $3 \times 3 \text{ mm}^2$ pixelated SiPM. In the bottom row, the difference in relative terms between the estimated resolution for the $3 \times 3 \text{ mm}^2$ SiPM and the $6 \times 6 \text{ mm}^2$ one.

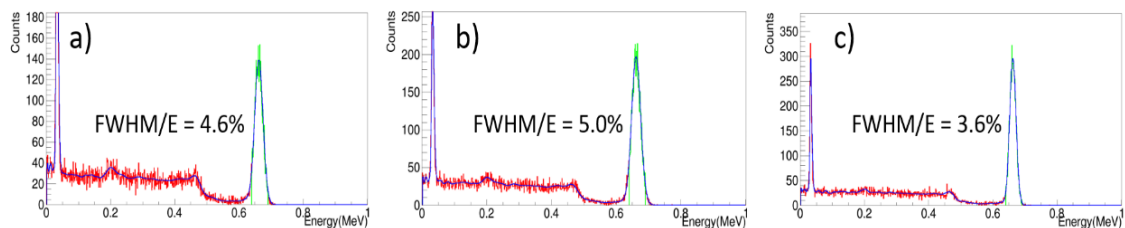


Fig. 24.- Optical MC simulation of the response function for the three crystals with thicknesses of 10 mm (a), 20 mm (b) and 30 mm (c), each readout with a 16×16 channel SiPM with a pixel size of $3 \times 3 \text{ mm}^2$. See text for details.

We find the rather surprising result that, the energy resolution is only marginally affected by the thinner pixel-size, despite of the larger dead-space when compared to the $6 \times 6 \text{ mm}^2$ pixel. This effect can be understood by the fact that the loss in resolution is proportional to the square-root value of the ratios between the dead-zones for the low- and high-granularity SiPMs, which is much smaller than the simple ratio of the dead-zones for each SiPM.

In summary, there are essentially two aspects to consider regarding the usefulness of the 3 mm pixel size for the iTED design, namely, the higher complexity in readout- and processing electronics, which need to be scaled by a factor of four to use 3x3 mm² pixels compared to the instrumentation required for the 6x6 mm² pixels, and the performance of the thinner pixel in terms of spatial sensitivity, both on the XY-plane and DOI. The latter aspects are discussed in the section below.

5.2.- SPATIAL RESPONSE

The spatial distribution of the scintillation light distribution along the transversal XY-plane of the crystal is displayed in Fig. 25 at the example of a 511 keV pencil-beam impinging on the center of the crystal. In order to illustrate the effect of the pixel size, the simulation has been carried out for an artificially small pixel size (without dead zones) of 1x1 mm² (Fig. 25-a,d), and for commercially available SiPMs with granularities of 3x3 mm² (with a pitch length between pixels of 3.37 mm)(Fig. 25-b,e) and 6x6 mm² (with a pitch length between pixel of 6.33)(Fig. 25-c,f).

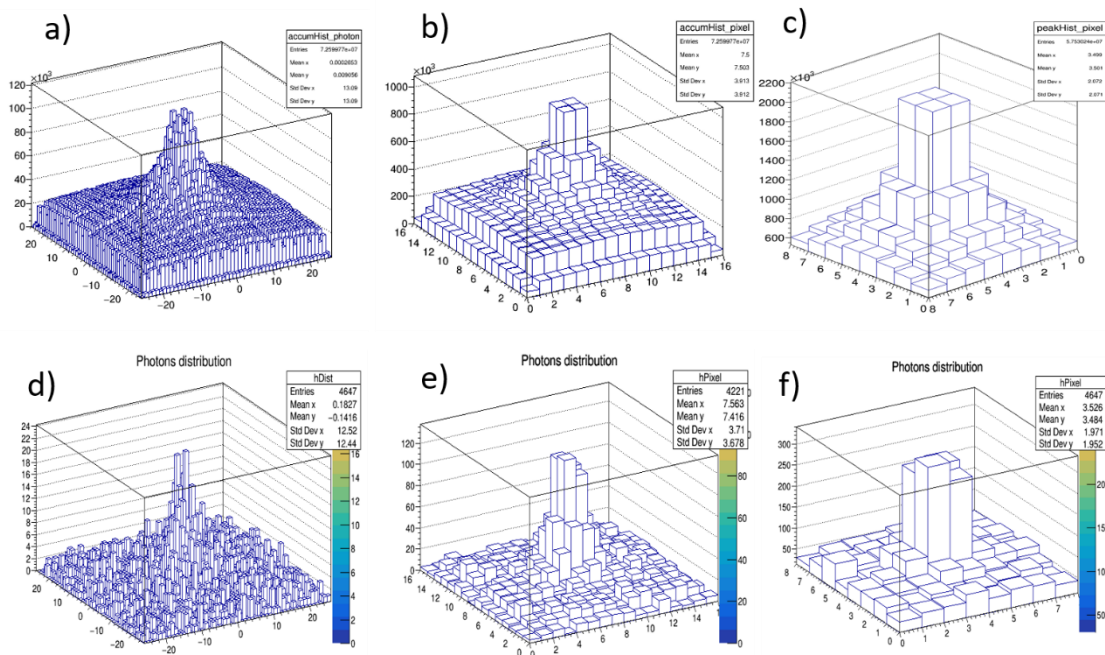


Fig. 25.- (Top row) Accumulated spatial distribution of scintillation photons over the SiPM surface displayed with an artificially thin granularity of 1x1 mm² (a), 3x3 mm² (b) and 6x6mm² (c). (Bottom row) Same as above, for one single interaction in the central region of the crystal, which illustrates the statistical pixel fluctuations that are expected on an event-by-event basis.

From the simulation we find a distribution with an average FWHM of 31 mm, which is substantially larger than the 6 mm pixel size, thus indicating a reasonable sampling resolution for deriving accurately the position coordinates X and Y. Indeed, similar light-sampling resolutions have led in the past to satisfactory position reconstruction results [8] [9]. Inspection of the same distribution for a single gamma-ray interaction in the central region of the crystal

indicates that the 6 mm pixel-size distribution is better defined (Fig. 25-d), owing to the lower statistical fluctuations when compared to the artificially thin 1 mm distribution (Fig.25-c). Indeed, the latter would require some sort of re-binning in order to properly define the maximum of the distribution.

Various algorithms have been implemented in order to obtain the desired information about the gamma-interaction coordinates from light distribution (see Appendix B).

The Anger technique approach consists on taking the X and Y mean values of the light distribution in order to specify X and Y coordinates of the gamma-ray interaction point. The depth of interaction DOI might be obtained by analysing the dependence of the standard deviation (FWHM) of the distribution with DOI, as it is expected that an interaction close to the surface gives as result a narrow distribution around the X and Y position of the interaction point. For a larger distance between detecting surface and interaction point, as optical path is also larger, photons are distributed over a wider surface then increasing the light-distribution standard deviation. A more accurate method to infer the interaction point would be based on the same algorithm but using the square values of the light distribution. This method is known as Pani technique.

Assuming that the scintillation photons are emitted isotropically and from a punctual light-source, an analytic model for the light distribution over the photosensor surface gives us the amount of light that can be detected at an arbitrary point located on the detecting surface [58]. This quantity will depend on the distance between the gamma-ray interaction point and the position at the entrance window where light is detected. Taking into account that light propagation obeys geometrical optics and the inverse square law, at the observation point \vec{r} one obtains the following intensity:

$$L(\vec{r}) = \frac{L_0}{(\vec{r}-\vec{r}_0)^2} \alpha e^{\alpha|\vec{r}-\vec{r}_0|} + \tau \quad (15)$$

where \vec{r}_0 are the coordinates of the gamma-interaction point, L_0 is the overall released light intensity, α is a parameter that takes into account possible absorption and scattering processes and τ in a constant reflecting the light background.

We have implemented the last result as a user defined function in ROOT with the aim of being able to fit it, based on a least-squares minimization, with the light distribution obtained by MC simulations, what should give us the values of the coordinates \vec{r}_0 . In Fig. 26 an example of the fit achieved (red mesh) by this means is shown. Using this analytical model has revealed itself as a more accurate and sophisticated way of obtaining the information of the X and Y coordinates of the gamma-interaction point along with its Depth Of Interaction than for example using a Gaussian distribution as a fitting function.

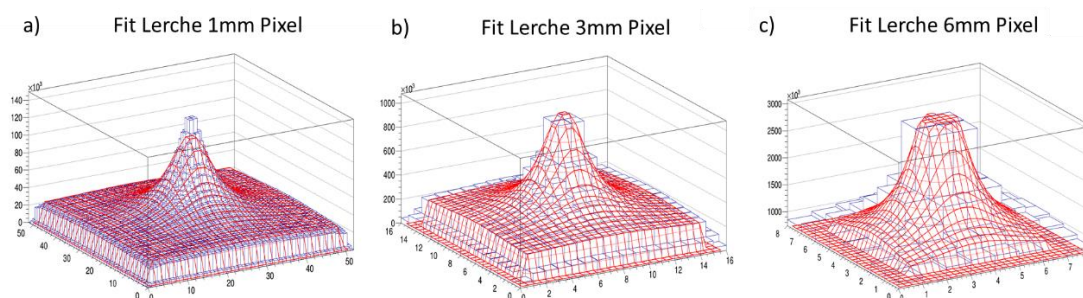


Fig. 26.- Fit of the analytical model of the light distribution (red mesh) to the accumulated light distribution coming out from simulations for a) 1x1 mm² pixel size, b) 3x3 mm² pixel size and c) 6x6 mm² pixel size.

In order to study the impact of the pixelation granularity on the position resolution we have applied the exposed algorithms to the distributions resulting from the simulation of a pincel-beam impinging on the center of the 20 mm thick detector coupled to a SiPM with pixel sizes of 1mm, 3mm and 6mm and also for pincel-beams impinging over the diagonal of the detector.

5.2.1.- XY RESPONSE

A.- ANGER TECHNIQUE

The results obtained with the Anger-like technique for a pincel-beam impinging on the center of the 20 mm thick detector are exposed in table 4 and shown in Fig.27 along the X direction.

Mean Value		FWHM		FWTM	
X(mm)	Y(mm)	X(mm)	Y(mm)	X(mm)	Y(mm)
-0.010(9)	0.000(9)	0.7(2)	0.7(2)	1.7(2)	1.7(2)
-0.011(9)	0.002(9)	0.7(2)	0.7(2)	1.7(2)	1.7(2)
-0.009(9)	0.001(9)	0.6(2)	0.7(2)	1.7(2)	1.8(2)

Table 4. Mean values, Full Width Half Maximum and Full Width Tenth Maximum obtained from the light distribution along X and Y directions of the photosensor, for a gamma-ray impinging in the centre of the crystal. The values were obtained using the Anger technique and considering 1x1 mm² (first row), 3x3 mm²(second row) and 6x6 mm²(third row) pixel granularity of the SiPM.

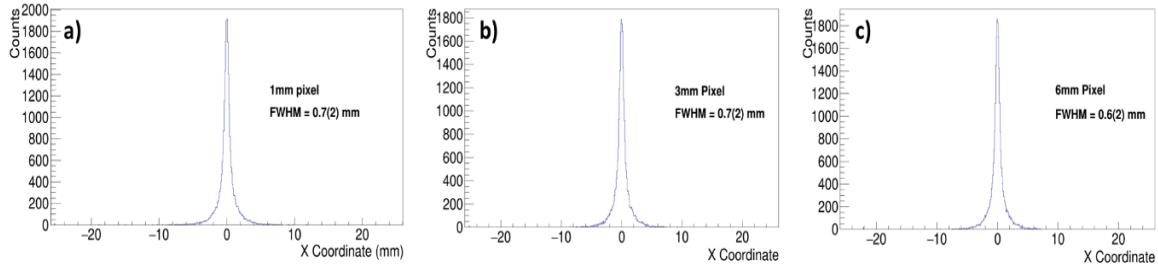


Fig. 21.- Position reconstruction along the X direction for a gamma-ray impinging in the center of the 20 mm thick crystal using the Anger technique. The results were obtained for the 1x1 mm² pixel size(a), 3x3 mm² pixel size(b) and 6x6mm² pixel size(c).

As expected, no clear trend or improvement is found when decreasing the pixel size for the reconstruction of the gamma-ray interaction coordinates across the transversal crystal plane XY for a gamma-ray impinging in the centre of the crystal. For gamma-rays impinging close to the border of the crystal, a poorer reconstruction of the interaction point is expected. To analyse this fact, we performed simulations of gamma-rays impinging perpendicularly to the front face of the detector on the positions X = Y= 12.66 mm and X = Y = 21.155 mm. In the table 5 we show the results obtained for the latter case, and in Fig. 28 can be seen the representation of the mean values obtained along the X direction.

Mean Value		FWHM		FWTM	
X(mm)	Y(mm)	X(mm)	Y(mm)	X(mm)	Y(mm)
6.929(8)	6.949(8)	0.6(2)	0.6(2)	1.3(2)	1.3(2)
6.935(9)	6.954(9)	0.6(2)	0.6(2)	1.4(2)	1.3(2)
6.907(9)	6.929(9)	0.7(2)	0.7(2)	1.3(2)	1.3(2)

Table 5. Mean values, Full Width Half Maximum and Full Width Tenth Maximum obtained from the light distribution along X and Y directions of the photosensor, for a gamma-ray impinging perpendicularly on X = Y = 21.155 mm. The values were obtained using the Anger technique and considering 1x1 mm² (first row), 3x3 mm²(second row) and 6x6 mm²(third row) pixel granularity for the SiPM.

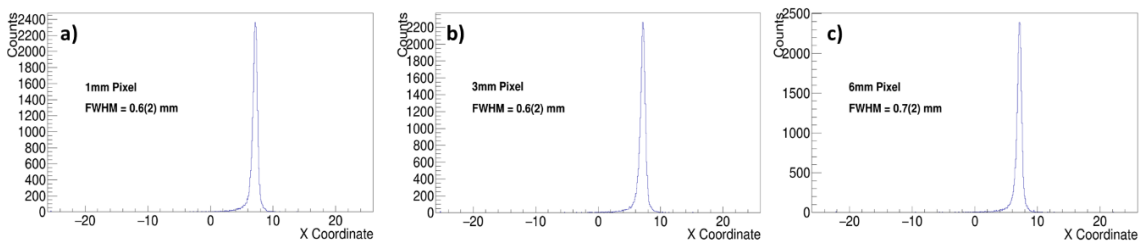


Fig. 28.- Position reconstruction along the X direction for a gamma-ray impinging in the corner of the 20 mm thick crystal using the Anger technique. The results were obtained for the 1x1 mm² pixel size(a), 3x3 mm² pixel size(b) and 6x6mm² pixel size(c).

In this case, we do not find any substantial difference using different pixel granularities. As can be seen, using mean values for the reconstruction of the X and Y coordinates of the interaction point is not an accurate method when moving to the borders of the crystal. In an ideal situation, the representation of the reconstructed interaction point versus the real interaction point along the XY plane would be the bisector line in the first and third quadrants. In Fig. 29 we show the latter representation for three different points along the diagonal of the detector at 0 mm, 17.437 mm (distance from the centre to the point X = 12.66, Y =12.66) and 29.918 mm (distance from the centre to the point X = 21.155, Y =21.155).

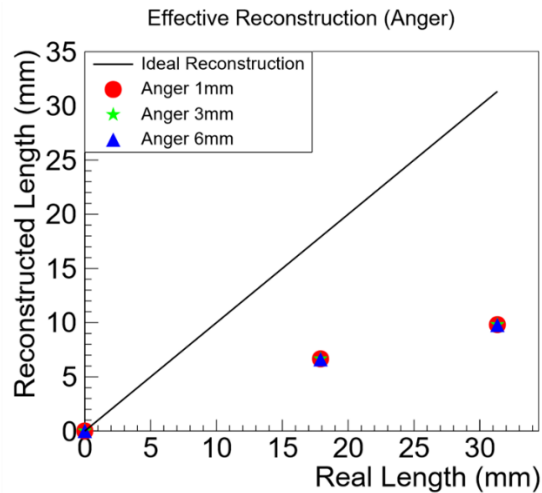


Fig. 29.- Spatial reconstruction of the gamma-ray interaction points impinging at the points X = Y = 0 mm, X = Y = 12.33mm and X = Y = 21.155 using the Anger technique.

In the latter figure it is reflected the similar response for all the pixel granularity modelled and the lack of accuracy when trying to reconstruct the real interaction point along the XY transversal plane.

B.- PANI TECHNIQUE

With this technique, we expect a better reconstruction of the X and Y interaction coordinates as the intensities are weighted and the points with a higher intensity measured are benefited. Results for a centered gamma-ray in the crystal are exposed in table TAB and the X mean value distributions are shown in figure FIG. In both cases once again we made the analysis for the 1x1 mm², 3x3 mm² and 6x6 mm² crystals (20 mm thicknesses).

Mean Value		FWHM		FWTM	
X(mm)	Y(mm)	X(mm)	Y(mm)	X(mm)	Y(mm)
-0.008(13)	0.008(13)	0.7(2)	0.7(2)	1.9(2)	2.1(2)
0.009(15)	0.023(15)	0.9(2)	0.8(2)	2.5(2)	2.2(2)
0.004(16)	0.016(16)	0.8(2)	0.9(2)	2.2(2)	2.4(2)

Table 6. Mean values, Full Width Half Maximum and Full Width Tenth Maximum obtained from the light distribution along X and Y directions of the photosensor, for a gamma-ray impinging perpendicularly on the centre of the crystal. The values were obtained using the Pani technique and considering 1x1 mm² (first row), 3x3 mm² (second row) and 6x6 mm² (third row) pixel granularity of the SiPM.

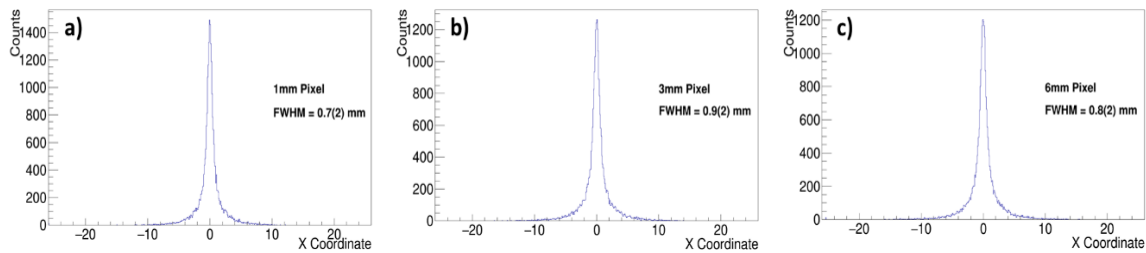


Fig. 30.- Position reconstruction along the X direction for a gamma-ray impinging in the centre of the 20 mm thick crystal using the Pani technique. The results were obtained for the 1x1 mm² pixel size(a), 3x3 mm² pixel size(b) and 6x6mm² pixel size(c).

As expected we do not find a substantial difference neither. However, a small discrepancy can be seen in the reconstruction of the Y coordinate for the 3x3 mm² and 6x6 mm² crystals as they show a slightly higher value. This can be understood as an effect of squaring the light distribution which introduces differences due to the probabilistic nature of Monte Carlo simulations. If we move to the vertex of the crystal as we made for the Anger-technique study, larger differences arise as can be seen in table 7 and figure Fig.31.

Mean Value		FWHM		FWTM	
X(mm)	Y(mm)	X(mm)	Y(mm)	X(mm)	Y(mm)
12.407(18)	12.433(17)	2.2(2)	1.9(2)	5.9(2)	5.5(2)
14.031(16)	14.059(15)	1.2(2)	1.2(2)	3.1(2)	3.2(2)
15.131(16)	15.166(16)	1.1(2)	1.2(2)	2.6(2)	2.8(2)

Table 7. Mean values, Full Width Half Maximum and Full Width Tenth Maximum obtained from the light distribution along X and Y directions of the photosensor, for a gamma-ray impinging perpendicularly on X = Y = 21.155 mm. The values were obtained using the Anger technique and considering 1x1 mm² (first row), 3x3 mm² (second row) and 6x6 mm² (third row) pixel granularity of the SiPM.

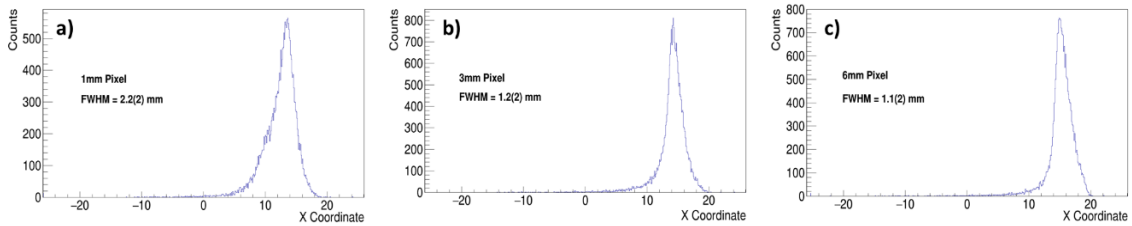


Fig. 31.- Position reconstruction along the X direction for a gamma-ray impinging in the corner of the 20 mm thick crystal using the Pani technique. The results were obtained for the 1x1 mm² pixel size(a), 3x3 mm² pixel size(b) and 6x6mm² pixel size(c).

Two important aspects can be seen in the latter results. In one hand, we find that the position reconstruction gets better for bigger pixel size (mean values are closer to the interaction point). In the other hand, the distribution of the mean values obtained is narrower also for bigger pixel sizes, this is, the spatial resolution gets better. In order to explain this fact (a better resolution was supposed to be found for smaller granularities), let us suppose two situations as depicted in figure Fig. 32, in which three photons reach to two photosensors with 4 and 2 pixels respectively.

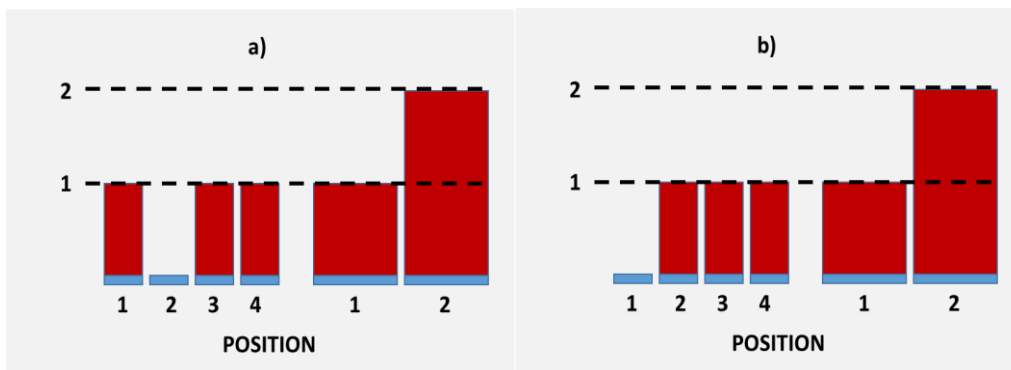


Fig. 32.- Two examples of three photons reaching two photosensors with different granularities. Cases a) and b) lead to a different distribution of the mean value for the small granularity while the distribution would be the same for the photosensor with a larger granularity.

In the first case (FIG. 31-a) for the small granularity we would obtain a mean value of $\frac{1+3+4}{3} = 2.667$ a.u. on the first event and a mean value of $\frac{2+3+4}{3} = 3$ a.u. for the second event. Meanwhile, for the larger granularity in both cases we would obtain a mean value of $\frac{1+2*2}{3} = 1.667$ a.u. Thus, for a larger granularity, the distribution remains the same on both events and the FWHM will be zero. In the latter example, although the FWHM would be better for the larger pixel size, the small pixel granularity predicts a better reconstruction of the interaction point (that we can assume to happen in 3.5 a.u.). However, we exposed a really simple example in which there was not a big difference in the counts on the bigger pixels. A better statistic would

lead to a higher difference among them and this would help for a better prediction of the interaction point.

The same representation made in Fig. 29 but using the Pani technique is now shown in figure Fig. 33.

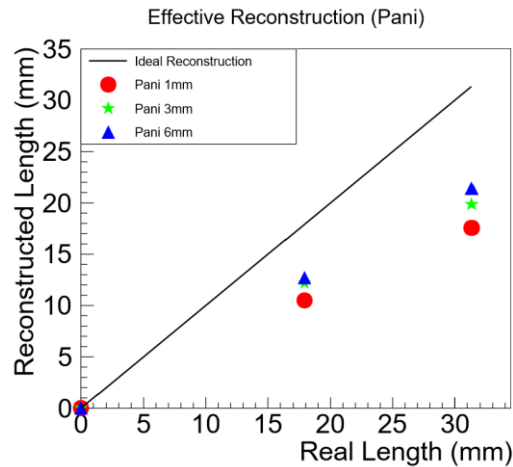


Fig. 33.- Spatial reconstruction of the gamma-ray interaction points impinging at the points $X = Y = 0$ mm, $X = Y = 12.33$ mm and $X = Y = 21.155$ using the Pani technique.

As it can be seen, this technique gives a better reconstruction of the interaction point with closest values to the ideal situation for the photosensor with 6×6 mm² pixel size. However, we do not find these results accurate enough for our purpose and we have investigated other techniques to obtain better results. This fact led us to develop what we have called Lerche technique based on the fit of the formula exposed in equation 15. Although we have not been able to develop a thorough analysis of the use of this technique, in figure Fig. 26 can be seen the promising results that could be obtained by fitting the light distribution to the analytical formula. The methodology that is intended to be carried out is to obtain a good sample of light distribution for an interaction in the center of the crystal and then displace the fitted function over the XY plane until a good fit is achieved for other interaction points. The coordinates \vec{r}_0 would give us promptly the interaction point of the reconstructed gamma-interaction.

5.2.2.- DEPTH OF INTERACTION

The reconstruction of the Depth Of Interaction has revealed itself as a difficult task in our work. Several strategies have been proposed in the development of this work, all of them based on the fact exposed in section Sec 5.2 that the width of the light distribution depends on the distance between the interaction point and the detecting surface. In this sense, future studies will be performed by analysing the dependence of the FWHM, FWTM and Standard Deviation of the light distribution with the depth of interaction. We have to remark that thanks to optical simulations, we can take advantage of the accessibility to the interaction point information in order to filter the events according to specific coordinates of the gamma-interactions. A first analysis of the standard deviation response, shown in table 7, was made by

using both the Anger- and Pani-technique for gamma rays impinging in the centre and the corner of the crystal.

Anger Technique				Pani Technique			
Centre		Corner		Centre		Corner	
σ_x (mm)	σ_y (mm)						
13.011(4)	13.008(4)	14.216(4)	14.211(4)	1.218(5)	1.210(5)	1.078(4)	1.075(4)
13.099(4)	13.096(4)	14.268(5)	14.268(5)	1.432(6)	1.427(6)	1.049(5)	1.049(5)
13.032(4)	13.026(4)	14.358(4)	14.358(4)	1.251(5)	1.244(6)	0.946(4)	0.934(4)

Table 7. Standard deviation obtained, on an event-by-event analysis, for the light distribution using both Anger- and Pani-technique. The calculations were made for the 1x1 mm² pixel size (first row), 3x3 mm² pixel size (second row) and for the 6x6 mm² pixel size (third row).

This study, as the one performed to obtain the mean value of the distribution was made on an event-by-event basis. This results will be focus of further studies in order to understand the differences shown. The next step would be to obtain the FWHM and FWTM of the event-by event standard deviation in order to analyse the best technique and the most sensitive pixel granularity in order to get reliable results. We also expect good results by applying the aforementioned Lerche technique which, as mentioned before, would give us direct values of both XY- and depth-of- interaction point. Finally, the option of using Neural Networks for the position reconstruction is also being developed at the present.

6.- CONCLUSIONS

One of the most important results of this work concerns the fact, that we have demonstrated that the very demanding MC simulation of the scintillation photons can be carried out using modern computers (commonly available nowadays with i7 core) in combination with the latest Geant4 version implementing the recently available multithread capabilities. It is worth noting that this approach, which is now readily available for the user, would require until only recently a very large amount of CPUs (a farm), and an external methodology of parallelization.

A second important result from this work is related to the fact, that by means of optical MC simulation we have been able to achieve a level of accuracy in the reproduction of the energy response-function, which shows a rather good agreement with experimentally measured response functions. It is thus important to remark, that now one can rely and use the developed code in order to explore almost any kind of detector configuration, both in terms of detector size, thickness, finishing, as well as for different types of photosensor pixelations. This, in turn, translates into the possibility of reliably designing the experimental set-up for the objectives of the HYMNS project.

From the good agreement obtained for the spectroscopic response of this kind of detectors, one may expect also a rather reasonable agreement for the simulated spatial distribution of the scintillation light distribution. This feature enables the opportunity to develop sophisticated position-reconstruction algorithms, such as those mentioned in the section above, and also others based on Neural-Networks. The latter will be the focus of another study within HYMNS in the near future.

From the technical point of view, it is important to remark the result that, the energy resolution of large monolithic crystals does not deteriorate when using SiPM readout instead of conventional PMTs. On the contrary, using the latest Si-technology available, which features a large fill-factor (of APDs) and high quantum-efficiency, it becomes possible to even improve state-of-the-art results obtained with PMTs. Given the quick evolution and progress of SiPMs, one may even expect a further improvement with the next generation of SiPMs, an hypothesis, that can be tested with the developed MC code, once the features of the new SiPM are made available by the manufacturers.

In summary, we have developed the largest monolithic position-sensitive lanthanum halide with SiPM readout detector reported thus far. These detectors are intended for the deployment of a total-energy detector with imaging capability (i-TED) for radiative neutron capture experiments at TOF facilities. The developed MC code allows us to reproduce fairly well the spectroscopic and spatial behavior of our detectors. According to our calculations a thinner pixel size of 3 mm is not expected to provide any improvement in energy- or position-resolution, thus disregarding it for our application. Regarding the spatial sensitivity across the crystal thickness, we have seen that for the reconstruction of the X and Y coordinates of the gamma-ray interaction point, neither the Anger- nor the Pani-technique is accurate enough for our purpose. The use of the analytical model of the light distribution within the detecting surface is expected to reveal good results for the reconstruction of X, Y and Z coordinates.

Finally, we would like to mention that in order to perform detailed comparisons of the simulated pincel-beams impinging all over the crystal surface, during the development of this work, an XY-table has been designed and assembled by using an Arduino Nano microcontroller. However, and due to logistic issues, the measurements cannot have been performed yet.

CONCLUSIONES

Uno de los resultados más importantes de este trabajo se refiere al hecho de que hemos demostrado que la simulación Monte Carlo de fotones ópticos, que requieren un alto coste computacional, puede ser llevada a cabo usando modernos pero comunes ordenadores en combinación con las habilidades multi-hilo que ofrece la última versión de Geant4. Cabe mencionar que esta aproximación, al alcance de la mano de cualquier usuario, requeriría hasta hace poco tiempo el uso de una granja con un alto número de ordenadores y un método de paralelización externo.

Un segundo resultado importante está relacionado con el hecho de que, mediante la simulación óptica Monte Carlo, hemos logrado alcanzar un alto nivel de precisión a la hora de reproducir la respuesta energética que muestran las medidas realizadas experimentalmente. Es importante remarcar que ahora es posible utilizar el código implementado para explorar casi cualquier configuración prevista para el desarrollo del detector, tanto en términos de tamaño del cristal como en su acabado o en las diferentes pixelaciones del fotosensor que se quieran modelar. Esto se traduce a su vez en la posibilidad de llevar a cabo un diseño efectivo de la mejor configuración experimental para los objetivos marcados dentro del proyecto HYMNS.

Gracias al buen acuerdo obtenido en la respuesta espectroscópica en este tipo de detectores, cabe esperar también un acuerdo razonable a la hora de simular la distribución espacial de los fotones de centelleo. Esta característica nos da la oportunidad de desarrollar sofisticados algoritmos de reconstrucción de la posición, como los mencionados en las secciones anteriores y otros basados en redes neuronales. Éstas últimas serán objeto de estudio dentro del proyecto HYMNS en un futuro inmediato.

Desde un punto de vista técnico, es importante remarcar el resultado obtenido de que la respuesta energética de los cristales centelleadores monolíticos de gran tamaño no se verán deteriorados al usar fotomultiplicadores de silicio en vez de los tubos fotomultiplicadores convencionales. Al contrario, con el uso de la última tecnología de silicio disponible, caracterizada por un alto factor de llenado (de fotodiodos de avalancha) y una alta eficiencia cuántica, es posible llegar a mejorar los resultados obtenidos con los tubos fotomultiplicadores. Dada la rápida evolución y progreso en el desarrollo de los fotomultiplicadores de silicio, cabe esperar una rápida evolución en las nuevas generaciones de estos dispositivos, una hipótesis que puede ser contrastada con el código Monte Carlo implementado una vez las nuevas generaciones estén disponibles.

En resumen, hemos desarrollado el estudio energético y espacial del mayor detector sensible a la posición formado por un cristal monolítico de cloruro de lantano y acoplado a un fotomultiplicador de silicio hasta la fecha. Estos detectores serán la base del desarrollo de un Detector de Energía Total con habilidades de visualización (i-TED) para la medida de capturas neutrónicas radiativas en instalaciones tipo TOF ó Tiempo De Vuelo. El código Monte Carlo implementado nos ha permitido analizar la respuesta energética y espacial para pixelaciones de 3 mm y nos ha permitido llegar a la conclusión de que no cabe esperar una mejora sustancial en dichas respuestas. EN relación a la sensibilidad espacial a lo largo del detector, hemos observado que para la reconstrucción de las coordenadas X e Y del punto de interacción del rayo gamma en el cristal ni la técnica de Anger ni la de Pani es lo suficientemente precisa para nuestros propósitos. Esperamos que el uso del modelo analítico expuesto de la distribución de la luz a lo

largo de la superficie detectora arroje buenos resultados para la reconstrucción de las coordenadas X, Y y Z del punto de interacción.

Finalmente, nos gustaría mencionar que con el fin de desarrollar comparaciones precisas de las simulaciones realizadas para pinceles de rayos gamma incidiendo a lo largo de toda la superficie del detector, durante el desarrollo de este trabajo, también se ha diseñado y construido una mesa XY usando un microcontrolador Arduino Nano. Sin embargo, debido a problemas de logística, las medidas no han podido realizarse aún.

APPENDIX A. DATA ANALYSIS SCRIPTS

A.1 PMTModel.C

This script introduces the impact of the quantum efficiency of the PMT modelled in the simulation. The script generates an output file (`ph_File(PMT).vec`) containing the resulting energy spectra coming out from the simulations.

```
#include <fstream>

Double_t probability(Int_t nPhotons, Double_t qEff)
{
    return nPhotons*(qEff*pow(1-qEff,nPhotons-1));
}

int quantumE(){

    TH1F *hqe = new TH1F("hqe","Quantum efficiency",1000,0,10000);
    TH1F *hqPS = new TH1F("hqPS","Photosensor",1000,100,1100);

    TFile* f = new TFile("../OpSiPM_out.root");
    ofstream outputQE;
    outputQE.open("ph_File(PMT).vec");

    TTree *tEdep = (TTree*)f -> Get("Edep");
    TTree *tPInfo = (TTree*)f -> Get("PhotonInfo");

    Int_t phDtctd;
    Double_t phNrg;
    Int_t counts;

    tEdep -> SetBranchAddress("PhDetected",&phDtctd);

    tPInfo -> SetBranchAddress("Energy",&phNrg);

    Double_t xSpline[] = {250,300,350,400,450,500,550,600,650,725};
    Double_t ySpline[] = {0,0.13,0.23,0.3,0.23,0.17,0.09,0.033,0.009,0};

    grSpline = new TGraph(10,xSpline,ySpline);
    TSpline3* spline = new TSpline3("qeSpline",grSpline);
    TRandom* auxRndm = new TRandom();

    Int_t auxPhIter = 0;

    for (Int_t evtIter = 0; evtIter < tEdep -> GetEntries(); ++evtIter)
    {
        tEdep -> GetEntry(evtIter);

        counts = 0;

        for (Int_t phIter = auxPhIter; phIter < auxPhIter+phDtctd; ++phIter)
        {
            tPInfo -> GetEntry(phIter);
            if (auxRndm->Rndm() <= spline->Eval(4.1356733*pow(10,-
15)*3*pow(10,17)/(phNrg*pow(10,6))))
            {
                counts ++;
            }
        }
        auxPhIter += phDtctd;
        hqe -> Fill(counts);
    }
}
```

```

f -> Close();

Int_t bin;
Int_t content;

for (Int_t histIter = 0; histIter < hqe -> GetNbinsX(); ++histIter)
{
    bin = hqe -> GetBinCenter(histIter);
    content = hqe -> GetBinContent(histIter);
    outputQE << bin << "\t" << content << "\n";
}

outputQE.close();

for (Int_t qeIter = 250; qeIter <= 700; ++qeIter)
{
    hqPS -> SetBinContent(hqPS->FindBin(qeIter), spline->Eval(qeIter));
}

TCanvas *c = new TCanvas("c", "", 1);
hqPS -> Draw();

return 1;
}

```

A.2 SiPMModel.C

This script introduces the impact of both, the quantum efficiency and the existence of dead zones of the SiPM modelled in the simulation. The script generates an output file (`ph_File(SiPM).vec`) containing the resulting energy spectra coming out from the simulations.

```

#include <iostream>
#include <vector>
#include <stdlib.h>
#include <unistd.h>
#include "TFile.h"
#include "TTree.h"
#include "TRint.h"
#include <fstream>
#include "Photon.c"
#include "Gamma.c"
#include "Event.c"
#include <math.h>
#include "TH1F.h"
#include "TH2F.h"
#include "TH3F.h"
#include "TROOT.h"
#include "TSystem.h"
#include "TGraph.h"
#include "TRandom.h"
#include "TSpline.h"

using namespace std;

Bool_t isInPixel(Double_t xPos, Double_t yPos, Double_t * xCoord, Double_t
*yCoord, Int_t nPixels, Double_t pixelSize, Double_t pitch) {

    // Double_t xPos = photon.GetXPos();
    // Double_t yPos = photon.GetYPos();

```

Spatial And Spectroscopic Characterization of LaCl3 Crystals Coupled To Silicon Photosensors

```
Bool_t xInPixel = false;
Bool_t yInPixel = false;

Double_t xmin = -((nPixels - 1) * pitch + pixelSize) / 2;
Double_t ymin = xmin;

for (Int_t i = 0; i < nPixels; i++) {
    Double_t xInf = xmin + i * pitch;
    Double_t xSup = xmin + pixelSize + i * pitch;

    Double_t yInf = ymin + i * pitch;
    Double_t ySup = ymin + pixelSize + i * pitch;

    if ( xPos >= xInf && xPos <= xSup){
        xInPixel = true;
        *xCoord = i;
    }

    if ( yPos >= yInf && yPos <= ySup){
        yInPixel = true;
        *yCoord = i;
    }
}

if (xInPixel && yInPixel){
    return true;
} else {
    return false;
}
}

int pixel(){

    ofstream outputFVec;
    outputFVec.open("ph_File(SiPM).vec");

    TFile* f = new TFile("../Important_Simulations/30mm/OpSiPM_out.root");
    TFile* outputFile = new TFile("OpSiPM_pixel.root", "RECREATE");

    TTree *tEdep = (TTree*)f -> Get("Edep");
    TTree *tPinfo = (TTree*)f -> Get("PhotonInfo");

    int auxPhdtctd;

    double auxPxpos;
    double auxPypos;
    double auxPenergy;

    tEdep -> SetBranchAddress("PhDetected",&auxPhdtctd);

    tPinfo -> SetBranchAddress("Xposition",&auxPxpos);
    tPinfo -> SetBranchAddress("Yposition",&auxPypos);
    tPinfo -> SetBranchAddress("Energy",&auxPenergy);

    Int_t counts;

    TH1F* pHist = new TH1F("pHist","Photon spectra",4000,0,40000);

    Double_t pixelSize = 3.07;
    Double_t pitch = 3.36;

    Int_t nPixels = 16;

    Double_t xCoord = 10;

    Double_t yCoord = 10;
}
```

```

    Double_t xSpline[] = {250,300,350,400,450,500,550,600,650,700};
    Double_t ySpline[] =
    {0.05*46/50.,0.2*46/50.,0.375*46/50.,0.455*46/50.,0.52*46/50.,0.43*46/50.,0.27
    *46/50.,0.17*46/50.,0.15*46/50.,0.1*46/50.};

    TGraph* grSpline = new TGraph(10,xSpline,ySpline);
    TSpline3* spline = new TSpline3("qeSpline",grSpline);
    TRandom* auxRndm = new TRandom();

    Int_t auxPhIter = 0;

    for (Int_t treeIter = 0; treeIter < tEdep -> GetEntries(); ++treeIter)
    {
        tEdep -> GetEntry(treeIter);
        counts = 0;

        for(Int_t pIter = auxPhIter; pIter < auxPhIter+auxPhdtctd; ++pIter)
        {
            tPinfo -> GetEntry(pIter);
            if (auxRndm->Rndm() <= spline->Eval(4.1356733*pow(10,-
15)*3*pow(10,17)/(auxPenergy*pow(10,6))) &&
isInPixel(auxPxpos,auxPypos,&xCoord,&yCoord,nPixels,pixelSize,pitch))
            {
                counts ++;
            }
        }
        auxPhIter += auxPhdtctd;

        pHist -> Fill(counts);

        cout << "Processing Entry: " << treeIter << " out of: " << tEdep ->
GetEntries() << "\n" ;
    }

    cout << "Finished" << endl;
    cout << pHist -> GetNbinsX();

    for (Int_t histIter = 0; histIter < pHist->GetNbinsX(); ++histIter)
    {
        Int_t bin = pHist->GetBinCenter(histIter);
        Int_t content = pHist->GetBinContent(histIter);
        outputFVec << bin << "\t" << content << "\n";
    }

    outputFVec.close();
    f -> Close();
    outputFile -> Close();

    return 1;
}

```

A.3 processing.C

In this script, we introduce the effect of the quantum efficiency and the dead zones of the SiPM modelled and we link each photon detected to the pixel which it reaches. Doing so, we are able then to study the spatial response of the Position Sensitive Detector with the scripts described in the sections below.

```

#include <iostream>
#include <vector>
#include <stdlib.h>
#include <unistd.h>

```

Spatial And Spectroscopic Characterization of LaCl3 Crystals Coupled To Silicon Photosensors

```
#include "TFile.h"
#include "TTree.h"
#include "TRint.h"
#include <fstream>
#include <math.h>
#include "TH1F.h"
#include "TH2F.h"
#include "TH3F.h"
#include "TROOT.h"
#include "TSystem.h"
#include "TGraph.h"
#include "TRandom.h"
#include "TSpline.h"

using namespace std;

Bool_t isInPixel(Double_t xPos, Double_t yPos, Double_t* xCoord, Double_t*
yCoord, Int_t nPixels, Double_t pixelSize, Double_t pitch)
{
    Double_t xmin = ((nPixels-1)* pitch +pixelSize)/2;
    Double_t ymin = xmin;

    xPos += xmin;
    xPos /= pitch;
    yPos += ymin;
    yPos /= pitch;

    Double_t xPosRel = modf (xPos,xCoord);
    Double_t yPosRel = modf (yPos,yCoord);

    if (xPosRel >= 0 && xPosRel <= 1-(pitch-pixelSize)/pitch && yPosRel >= 0 &&
yPosRel <= 1-(pitch-pixelSize)/pitch ){
        return true;
    } else {
        return false;
    }
}

int processData(){

    // Open file coming from simulation

    Double_t pixelSize = 6.07;
    Double_t pitch = 6.33;

    Int_t nPixels = 8;

    TFile* f = new TFile("../OpSiPM_processed.root");

    // Output file

    TFile* outputFile = new TFile("OpSiPM_processed.root","RECREATE");

    // Old Trees

    TTree *tEdep = (TTree*)f -> Get("Edep");
    TTree *tGinfo = (TTree*)f -> Get("GammaInfo");
    TTree *tPinfo = (TTree*)f -> Get("PhotonInfo");

    // New tree

    TTree tSiPM("tSiPM","Events");

    // Variables to store data from trees

    double auxEdep;
```

```

int auxNint;
int auxPhgnrtd;
int auxPhdtctd;

int auxGInt;
double auxGedep;
double auxGtime;
double auxGxpos;
double auxGypos;
double auxGzpos;
Char_t auxGprocess;

double auxPxpos;
double auxPypos;
double auxPtime;
double auxPenergy;

Event event;

Int_t qePhotons;

Int_t counts[nPixels*nPixels];

TH1F* pixels[nPixels*nPixels];
for (Int_t histIter = 0; histIter < nPixels*nPixels; histIter++)
{
    Char_t histName[15] = {0};
    sprintf(histName,"pixl%iHist",histIter+1);
    pixels[histIter]=new TH1F(histName,histName,10000,0,20000);
}

Gamma auxGamma;
Photon auxPhoton;

std::vector<Gamma> auxVGamma;
std::vector<Photon> auxVPhoton;

// auxVGamma.reserve(30);
// auxVPhoton.reserve(1000);

TH2F* hPixel = new TH2F("hPixel","Photons
distribution",nPixels,0,nPixels,nPixels,0,nPixels);
TH2F* hDist = new TH2F("hDist","Photons distribution",52,-26,26,52,-26,26);
TH3F* hGInteraction = new TH3F("hGInteraction","Gamma Interactions",52,-
26,26,52,-26,26,30,0,30);

// Link variables to the input trees branches

tEdep -> SetBranchAddress("Edep",&auxEdep);
tEdep -> SetBranchAddress("NInteractions",&auxNint);
tEdep -> SetBranchAddress("PhGenerated",&auxPhgnrtd);
tEdep -> SetBranchAddress("PhDetected",&auxPhdtctd);

tGinfo -> SetBranchAddress("Interaction",&auxGInt);
tGinfo -> SetBranchAddress("Edep",&auxGedep);
tGinfo -> SetBranchAddress("Time",&auxGtime);
tGinfo -> SetBranchAddress("Xposition",&auxGxpos);
tGinfo -> SetBranchAddress("Yposition",&auxGypos);
tGinfo -> SetBranchAddress("Zposition",&auxGzpos);
tGinfo -> SetBranchAddress("Process",&auxGprocess);

tPinfo -> SetBranchAddress("Time",&auxPtime);
tPinfo -> SetBranchAddress("Xposition",&auxPxpos);
tPinfo -> SetBranchAddress("Yposition",&auxPypos);
tPinfo -> SetBranchAddress("Energy",&auxPenergy);

```

Spatial And Spectroscopic Characterization of LaCl3 Crystals Coupled To Silicon Photosensors

```
tSiPM.Branch("Event",&event,99);
tSiPM.Branch("Pixels",counts,"counts[2704]/I");
tSiPM.Branch("PixelDist",pixels);
tSiPM.Branch("PixelHist",&hPixel);
tSiPM.Branch("PhotonHist",&hDist);
tSiPM.Branch("GammaDist",&hGInteraction);

// Parameters defining the SiPM

Double_t xCoord = 10;

Double_t yCoord = 10;

// Block for the QE spline

Double_t xSpline[] = {250,300,350,400,450,500,550,600,650,700};
Double_t ySpline[] =
{0.05*46/50.,0.2*46/50.,0.375*46/50.,0.455*46/50.,0.52*46/50.,0.43*46/50.,0.27
*46/50.,0.17*46/50.,0.15*46/50.,0.1*46/50.};

TGraph* grSpline = new TGraph(10,xSpline,ySpline);
TSpline3* spline = new TSpline3("qeSpline",grSpline);
TRandom* auxRndm = new TRandom();

// Pixel mapping

int pixelMap [nPixels][nPixels];

for (Int_t rowIter = 0; rowIter < nPixels; ++rowIter)
{
    for (Int_t colIter = 0; colIter < nPixels; ++colIter)
    {
        pixelMap[rowIter][colIter] = (1+rowIter)+(colIter*nPixels);
    }
}

// Read and fill the tree

Int_t auxGIter = 0;
Int_t auxPhIter = 0;

Int_t auxEvtNumber = 0;

for (Int_t treeIter = 0; treeIter < tEdep -> GetEntries(); ++treeIter)
{
    auxEvtNumber ++;

    tEdep -> GetEntry(treeIter);

    event.evtNumber = auxEvtNumber;
    event.nInteractions = auxNint;
    event.eDep = auxEdep;
    event.phGenerated = auxPhgnrtd;

    auxVGamma.clear();
    for (Int_t gIter = auxGIter; gIter < auxGIter+auxNint; ++gIter)
    {
        tGinfo -> GetEntry(gIter);

        auxGamma.nInteraction = auxGInt;
        auxGamma.eDep = auxGedep;
        auxGamma.xPos = auxGxpos;
        auxGamma.yPos = auxGypos;
        auxGamma.zPos = auxGzpos;
        auxGamma.time = auxGtime;
        auxGamma.process = auxGprocess;
    }
}
```

```

    hGInteraction -> Fill(auxGxpos,auxGypos,auxGzpos);

    auxVGamma.push_back(auxGamma);
}
auxGIter += auxNint;
event.gammaInfo = auxVGamma;

auxVPhoton.clear();
qePhotons = 0;
for(Int_t pIter = auxPhIter; pIter < auxPhIter+auxPhdtctd; ++pIter)
{
    tPinfo -> GetEntry(pIter);
    if (auxRndm->Rndm() <= spline->Eval(4.1356733*pow(10,-
15)*3*pow(10,17)/(auxPenergy*pow(10,6))) &&
isInPixel(auxPxpos,auxPypos,&xCoord,&yCoord,nPixels,pixelSize,pitch))
    {
        auxPhoton.xPos = auxPxpos;
        auxPhoton.yPos = auxPypos;
        auxPhoton.time = auxPtime;
        auxPhoton.energy = auxPenergy;
        qePhotons ++;

        hPixel -> Fill(xCoord,yCoord);
        hDist -> Fill(auxPxpos,auxPypos);

        auxVPhoton.push_back(auxPhoton);

        counts[pixelMap[int(xCoord)][int(yCoord)]]++;
    }
}
for (Int_t pxIter = 0; pxIter < nPixels*nPixels; ++pxIter)
{
    pixels[pxIter] -> Fill(counts[pxIter]);
    counts[pxIter] = 0;
}
auxPhIter += auxPhdtctd;
event.photonInfo = auxVPhoton;
event.phDetected = qePhotons;

tSiPM.Fill();

for (Int_t pxIter2 = 0; pxIter2 < nPixels*nPixels; ++pxIter2)
{
    pixels[pxIter2] -> Reset();
}
hPixel-> Reset();
hDist -> Reset();
hGInteraction -> Reset();

    cout << "Processing Entry: " << treeIter << " out of: " << tEdep ->
GetEntries() << "\n" ;
}

outputFile -> Write();
outputFile -> Close();

f-> Close();

return 1;
}

```

A.4 spatialResponseAnger.c

With this script, we study the reconstruction of the interaction point along the X and Y axis by using the Anger-technique, the input file used is the one generated in section A.3.

```
#include "TMath.h"
#include "Event.h"
#include "Gamma.h"
#include "Photon.h"

R__LOAD_LIBRARY(Gamma_c.so)
R__LOAD_LIBRARY(Photon_c.so)
R__LOAD_LIBRARY(Event_c.so)

Double_t getFWHM(TH1D* inHisto){

    Double_t maxVal = inHisto->GetMaximum();
    Double_t minVal = inHisto->GetMinimum();
    Double_t halfMax = (maxVal + minVal)/2.;
    Int_t bin1 = inHisto->GetMaximumBin();
    Int_t bin2 = inHisto->GetMaximumBin();
    while (inHisto->GetBinContent(bin1)>=halfMax){
        bin1--;
    }
    while (inHisto->GetBinContent(bin1)>=halfMax){
        bin2++;
    }
    if(bin2>= bin1)
        return inHisto->GetBinCenter(bin2) - inHisto->GetBinCenter(bin1) +
2*inHisto->GetBinWidth(1);
    else
    {
        cout << " Warning bin2 < bin1 " << endl;
        return 0;
    }
}

Double_t getFWTM(TH1D* inHisto){

    Double_t maxVal = inHisto->GetMaximum();
    Double_t minVal = inHisto->GetMinimum();
    Double_t tenthMax = (maxVal + minVal)/10.;
    Int_t bin1 = inHisto->GetMaximumBin();
    Int_t bin2 = inHisto->GetMaximumBin();
    while (inHisto->GetBinContent(bin1)>=tenthMax){
        bin1--;
    }
    while (inHisto->GetBinContent(bin1)>=tenthMax){
        bin2++;
    }
    if(bin2>= bin1)
        return inHisto->GetBinCenter(bin2) - inHisto->GetBinCenter(bin1) +
2*inHisto->GetBinWidth(1);
    else
    {
        cout << " Warning bin2 < bin1 " << endl;
        return 0;
    }
}

void spatialResponse(){

    Int_t nPixel =8;
    Double_t pixelSize = 6.33;

    TFile* f = new TFile("../DataProcessing/OpSiPM_processed_6mm_35x_35y.root");
    TFile* outputFile = new TFile("../OpSiPM_spatialResponse.root","RECREATE");
```

```

TH2F* pixelHist = new TH2F("", "", nPixel, 0, nPixel, nPixel, 0, nPixel);
TH2F* hDist = new TH2F("hDist", "Photons distribution", 52, -26, 26, 52, -26, 26);
TH3F* gDist = new TH3F("", "", 52, -26, 26, 52, -26, 26, 30, 0, 30);

Event* event = new Event();

TTree* t = (TTree*) f->Get("tSiPM");
t -> SetBranchAddress("Event", &event);
t -> SetBranchAddress("GammaDist", &gDist);
t -> SetBranchAddress("PixelHist", &pixelHist);
t -> SetBranchAddress("PhotonHist", &hDist);

Double_t meanX = 0;
Double_t meanY = 0;
Double_t stdDevX = 0;
Double_t stdDevY = 0;
TH1D* hMeanX = new TH1D("hMeanX", "", 520, -26, 26);
TH1D* hMeanY = new TH1D("hMeanY", "", 520, -26, 26);
TH1D* hStdDevX = new TH1D("hStdDevX", "", 520, -26, 26);
TH1D* hStdDevY = new TH1D("hStdDevY", "", 520, -26, 26);

TTree* tInfo = new TTree("tInfo", "tInfo");
tInfo -> Branch("meanX", &meanX);
tInfo -> Branch("meanY", &meanY);

Int_t nEntries = t -> GetEntries();

for (Int_t treeIter = 0; treeIter < nEntries; ++treeIter){
    t -> GetEntry(treeIter);

    meanX = (pixelHist -> GetMean(1)-((nPixel-1)/2.))*pixelSize;
    meanY = (pixelHist -> GetMean(2)-((nPixel-1)/2.))*pixelSize;
    stdDevX = (pixelHist -> GetStdDev(1))*pixelSize;
    stdDevY = (pixelHist -> GetStdDev(2))*pixelSize;
    hMeanX -> Fill(meanX);
    hMeanY -> Fill(meanY);
    hStdDevX -> Fill(stdDevX);
    hStdDevY -> Fill(stdDevY);
    tInfo -> Fill();
}

cout <<"MEan (X): " << hMeanX -> GetMean() << endl;
cout <<"MEan (Y): " << hMeanY -> GetMean() << endl;
cout <<"MEan (X) Error: " << hMeanX -> GetMeanError() << endl;
cout <<"MEan (Y) Error: " << hMeanY -> GetMeanError() << endl;
cout <<"FWHM(x): " << getFWHM(hMeanX) << endl;
cout <<"FWHM(y): " << getFWHM(hMeanY) << endl;
cout <<"FWTM(x): " << getFWTM(hMeanX) << endl;
cout <<"FWTM(y): " << getFWTM(hMeanY) << endl;
cout <<"StdDev(x): " << hStdDevX->GetMean() << endl;
cout <<"StdDev(y): " << hStdDevY->GetMean() << endl;
cout <<"StdDev(x)Error: " << hStdDevX -> GetMeanError() << endl;
cout <<"StdDev(y)Error: " << hStdDevY -> GetMeanError() << endl;
outputFile -> Write();
outputFile -> Close();
f -> Close();
}

```

A.5 spatialResponsePani.C

With this script, we study the reconstruction of the interaction point along the X and Y axis by using the Pani-technique, the input file used is the one generated in section A.3.

```
#include "TMath.h"
#include "Event.h"
#include "Gamma.h"
#include "Photon.h"

R__LOAD_LIBRARY(Gamma_c.so)
R__LOAD_LIBRARY(Photon_c.so)
R__LOAD_LIBRARY(Event_c.so)

Double_t getFWHM(TH1D* inHisto){

    Double_t maxVal = inHisto->GetMaximum();
    Double_t minVal = inHisto->GetMinimum();
    Double_t halfMax = (maxVal + minVal)/2.;
    Int_t bin1 = inHisto->GetMaximumBin();
    Int_t bin2 = inHisto->GetMaximumBin();
    while (inHisto->GetBinContent(bin1)>=halfMax){
        bin1--;
    }
    while (inHisto->GetBinContent(bin1)>=halfMax){
        bin2++;
    }
    if(bin2>= bin1)
        return inHisto->GetBinCenter(bin2) - inHisto->GetBinCenter(bin1) +
2*inHisto->GetBinWidth(1);
    else
    {
        cout << " Warning bin2 < bin1 " << endl;
        return 0;
    }
}

Double_t getFWTM(TH1D* inHisto){

    Double_t maxVal = inHisto->GetMaximum();
    Double_t minVal = inHisto->GetMinimum();
    Double_t tenthMax = (maxVal + minVal)/10.;
    Int_t bin1 = inHisto->GetMaximumBin();
    Int_t bin2 = inHisto->GetMaximumBin();
    while (inHisto->GetBinContent(bin1)>=tenthMax){
        bin1--;
    }
    while (inHisto->GetBinContent(bin1)>=tenthMax){
        bin2++;
    }
    if(bin2>= bin1)
        return inHisto->GetBinCenter(bin2) - inHisto->GetBinCenter(bin1) +
2*inHisto->GetBinWidth(1);
    else
    {
        cout << " Warning bin2 < bin1 " << endl;
        return 0;
    }
}

void spatialResponsePani(){

    Int_t nPixel =8;
    Double_t pixelSize = 6.33;

    TFile* f = new TFile("../DataProcessing/OpSiPM_processed_6mm_35x_35y.root");
    TFile* outputFile = new TFile("../OpSiPM_spatialResponse.root","RECREATE");
```

```

TH2F* pixelHist = new TH2F("pixelHist","",nPixel,0,nPixel,nPixel,0,nPixel);
TH2F* hDist = new TH2F("hDist","Photons distribution",52,-26,26,52,-26,26);
TH3F* gDist = new TH3F("gDist","",52,-26,26,52,-26,26,30,0,30);

TH2F* auxHist = new TH2F("auxHist","",nPixel,0,nPixel,nPixel,0,nPixel);
TH2F* auxHist2 = new TH2F("auxHist2","",nPixel,0,nPixel,nPixel,0,nPixel);
Event* event = new Event();

TTree* t = (TTree*) f->Get("tSiPM");
t -> SetBranchAddress("Event",&event);
t -> SetBranchAddress("GammaDist",&gDist);
t -> SetBranchAddress("PixelHist",&pixelHist);
t -> SetBranchAddress("PhotonHist",&hDist);

Double_t meanX = 0;
Double_t meanY = 0;
Double_t stdDevX = 0;
Double_t stdDevY = 0;

TH1D* hMeanX = new TH1D("hMeanX","",520,-26,26);
TH1D* hMeanY = new TH1D("hMeanY","",520,-26,26);
TH1D* hStdDevX = new TH1D("hStdDevX","",520,-26,26);
TH1D* hStdDevY = new TH1D("hStdDevY","",520,-26,26);

TTree* tInfo = new TTree("tInfo","tInfo");
tInfo -> Branch("meanX",&meanX);
tInfo -> Branch("meanY",&meanY);

Int_t nEntries = t -> GetEntries();

for (Int_t treeIter = 0; treeIter < nEntries; ++treeIter){
  t -> GetEntry(treeIter);
  for (Int_t binIterX = 0; binIterX <= nPixel; ++binIterX){
    for (Int_t binIterY = 0; binIterY <= nPixel; ++binIterY){
      Int_t content = pixelHist -> GetBinContent(binIterX,binIterY)* pixelHist
-> GetBinContent(binIterX,binIterY);
      auxHist -> SetBinContent(binIterX,binIterY,content);
    }
  }
  meanX = ((auxHist -> GetMean(1))-((nPixel)/2.))*pixelSize;
  meanY = ((auxHist -> GetMean(2))-((nPixel)/2.))*pixelSize;
  stdDevX = (auxHist -> GetStdDev(1))*pixelSize;
  stdDevY = (auxHist -> GetStdDev(2))*pixelSize;

  hMeanX -> Fill(meanX);
  hMeanY -> Fill(meanY);
  hStdDevX -> Fill(stdDevX);
  hStdDevY -> Fill(stdDevY);
  tInfo -> Fill();
  pixelHist -> Reset();
  auxHist2 -> Add(auxHist);
  auxHist -> Reset();
}
auxHist2 -> Write();
cout <<"MeanX: " << hMeanX -> GetMean() << endl;
cout <<"MeanY: " << hMeanY -> GetMean() << endl;
cout <<"MeanX Error: " << hMeanX -> GetMeanError() << endl;
cout <<"MeanY Error: " << hMeanY -> GetMeanError() << endl;
cout <<"FWHM(x): " << getFWHM(hMeanX) << endl;
cout <<"FWHM(y): " << getFWHM(hMeanY) << endl;
cout <<"FWTM(x): " << getFWTM(hMeanX) << endl;
cout <<"FWTM(y): " << getFWTM(hMeanY) << endl;
cout <<"StdDev(x): " << hStdDevX->GetStdDev() << endl;
cout <<"StdDev(y): " << hStdDevY->GetStdDev() << endl;

```

```

cout <<"StdDevError(Y)" << hStdDevY -> GetStdDevError() << endl;
cout <<"StdDevError(X)" << hStdDevX -> GetStdDevError() << endl;
outputFile -> Write();
outputFile -> Close();
f -> Close();
}

```

A.6 fitLerche.C

This script was used in order to study the feasibility of using the analytical model of the light distribution within the crystal as a new method to reconstruct the gamma-ray interaction point.

```

#include "Event.h"
#include "Gamma.h"
#include "Photon.h"

Double_t lerche(Double_t *x, Double_t *par){

    // Double_t r_ro[3] = {x[0]-par[2],x[1]-par[3],23.6-par[4]};
    Double_t r_ro[3] = {x[0]-par[2],x[1]-par[3],-par[4]};
    Double_t mod_r_ro =
    TMath::Sqrt(r_ro[0]*r_ro[0]+r_ro[1]*r_ro[1]+r_ro[2]*r_ro[2]);
    Double_t mod_r_ro_2 = mod_r_ro*mod_r_ro;
    Double_t L = 0;
    Double_t tau = par[5];
    //if(par[4] > 3.6)
    if(par[4] > 0)
        L = par[0]/mod_r_ro_2*par[1]*TMath::Exp(-1.*par[1]*mod_r_ro) + par[5];
    //    L = par[0]/mod_r_ro_2*par[1]*TMath::Exp(-1*par[1]*mod_r_ro) +
    par[5];

    return L;
}

void fitLerche(){

    TFile* f = new TFile("./OpSiPM_processed_6mm.root");
    TFile* outputFile= new TFile("./OpSiPM_lerche.root","RECREATE");

    TTree* t = (TTree*)f -> Get("tSiPM");

    Event* event = new Event();
    TH2F* hPixel = new TH2F("hPixel","",8,0,8,8,0,8);
    TH3F* hGamma = new TH3F();

    TH2F* hAccum = new TH2F("hAccum","",8,0,8,8,0,8);

    TF2* func_pixel = new TF2("fit_pixel",lerche,1,7,1,7,6);
    func_pixel -> SetParNames("lL0","alpha","x0","y0","z0","tau_bkg");

    t -> SetBranchAddress("PixelHist",&hPixel);
    t -> SetBranchAddress("Event",&event);
    t -> SetBranchAddress("GammaDist",&hGamma);

    for (Int_t treeIter = 0; treeIter < t -> GetEntries(); ++treeIter){
        t -> GetEntry(treeIter);
        hAccum -> Add(hPixel);
        hPixel -> Reset();
    }

    func_pixel -> SetParameters(1E3*hAccum->GetMaximum(),9E-2,hAccum-
    >GetMean(1),hAccum->GetMean(2),10,hAccum->GetMinimum());
}

```

```
hAccum -> Fit("fit_pixel","R");

cout << "x0= " << func_pixel-> GetParameter(2)-26<< ", y0 = " << func_pixel-
> GetParameter(3)-26<< ", z0 = " << func_pixel-> GetParameter(4) << endl;

cout << "xPos= " << event->gammaInfo[0].xPos << ", yPos= " << event-
>gammaInfo[0].yPos << ", zPos = " << event->gammaInfo[0].zPos << endl;

outputFile -> Write();
outputFile -> Close();
f -> Close();
}
```

FIGURE INDEX

- Fig. 1** a) Curve of atomic abundances. *Source: reference [16]*
b) Features of the curve of atomic abundances. *Source: reference [16]*
- Fig. 2** a) Hertzsprung-Russell diagram. *Source: https://en.wikipedia.org/wiki/Hertzsprung%E2%80%93Russell_diagram*
b) Origin of the elements (Big Bang and stellar nucleosynthesis). *Source: <https://en.wikipedia.org/wiki/Nucleosynthesis>*
- Fig. 3** Neutron capture scheme. *Source: <http://nmi3.eu/neutron-research/techniques-for-chemical-analysis.html>*
- Fig. 4** Representation of r- and s- process chains on the chart of nuclides. *Source: Adapted from <http://people.physics.anu.edu.au/~ecs103/chart/>*
- Fig. 5** Neutron-capture cross-section times atomic abundances in the solar system as a function of the mass number. *Source: reference [18]*
- Fig. 6** Detail of the ⁷⁹Se branching point. *Source: Adapted from <http://people.physics.anu.edu.au/~ecs103/chart/>*
- Fig. 7** Schematic view of the i-TED detection system. *Source: reference [5]*
- Fig. 8** Picture of the i-TED prototype under development. *Source: Own source.*
- Fig. 9** Reconstruction of the Compton cone based on two gamma-ray interactions in scatter PSD and absorber PSD respectively. *Source: reference [45]*
- Fig. 10** a) Impact of the uncertainties in imaging capabilities performance. *Source: Own source.*
b) Spatial distribution of the reconstructed interaction point along X axis. *Source: reference [45]*
- Fig. 11** a) Impact on the reconstruction of the gamma-ray interaction point when varying the energy resolution. *Source: reference [45]*
b) Impact on the reconstruction of the gamma-ray interaction point when varying the spatial resolution. *Source: reference [45]*
- Fig. 12** LaCl₃(Ce) crystal with dimensions 50 x 50 x 20 mm³ used in the measurements performed in the laboratory. *Source: Own source.*
- Fig. 13** Photomultiplier Tube Hamamatsu R6236 and 50 x 50 x 30 mm³ LaCl₃(Ce) Crystal used to analyse its spectroscopic response. *Source: Own source.*
- Fig. 14** Pixelated SiPM SensL and ASIC based frontout electronics model ArrayJ-60035-64P-PCB. *Source: Own source.*
- Fig. 15** TOFPET2 ASIC used in the measurements performed to analyse the spatial response of the detector. *Source: Own source.*

- Fig. 16** Calibrated energy spectra for the ^{137}Cs source measured with $\text{LaCl}_3(\text{Ce})$ crystals of different thicknesses and coupled to both, PMT and SiPM photosensors. *Source: Own source.*
- Fig. 17** Energy resolution comparison for different $\text{LaCl}_3(\text{Ce})$ crystals thicknesses coupled to both PMT and SiPM photosensors. *Source: Own source.*
- Fig. 18** a) Description of the detector geometry implemented in the simulation. *Source: Own source.*
 b) Simulation of a gamma-ray interaction within the sensitive volume of the detector. *Source: Own source.*
- Fig. 19** a) Scintillation light distribution implemented in the simulation. *Source: Own source.*
 b) Refractive index distributions implemented in the simulation for different materials. *Source: Own source.*
 c) Absorption length distributions implemented in the simulation for different materials. *Source: Own source.*
 d) Reflectivity distributions implemented in the simulation for different materials. *Source: Own source.*
- Fig. 20** Quantum efficiency for the two photosensors used in this study, as provided by the manufacturer and implemented in the code. *Source: Own source.*
- Fig. 21** a) CPU computation time (s) as a function of the number of simulated optical photons. *Source: Own source.*
 b) Average CPU time required for each optical photon, as a function of the number of threads. *Source: Own source.*
- Fig. 22** Spectroscopic response obtained from the Monte Carlo simulations and measurements. *Source: Own source.*
- Fig. 23** Comparison of experimental energy resolution versus optical MC simulated values. *Source: Own source.*
- Fig. 24** Spectroscopic response of $\text{LaCl}_3(\text{Ce})$ crystals of different thicknesses coupled to a 16x16 channel SiPM with a pixel size of $3\times 3\text{ mm}^2$. *Source: Own source.*
- Fig. 25** Accumulated spatial distribution of scintillation photons over the SiPM surfaces with different granularities. *Source: Own source.*
- Fig. 26** a) Analytical model function fitted to the accumulated light distribution for the 1mm pixilation granularity. *Source: Own source.*
 b) Analytical model function fitted to the accumulated light distribution for the 3mm pixilation granularity. *Source: Own source.*
 c) Analytical model function fitted to the accumulated light distribution for the 6mm pixilation granularity. *Source: Own source.*
- Fig. 27** a) Position reconstruction along the X direction of a gamma-ray impinging in the centre of the crystal, for the 1mm pixel size SiPM and using the Anger technique. *Source: Own source.*

b) Position reconstruction along the X direction of a gamma-ray impinging in the centre of the crystal, for the 3mm pixel size SiPM and using the Anger technique.
Source: Own source.

c) Position reconstruction along the X direction of a gamma-ray impinging in the centre of the crystal, for the 3mm pixel size SiPM and using the Anger technique.
Source: Own source.

Fig. 28 a) Position reconstruction along the X direction of a gamma-ray impinging in the corner of the crystal, for the 1mm pixel size SiPM and using the Anger technique.
Source: Own source.

b) Position reconstruction along the X direction of a gamma-ray impinging in the corner of the crystal, for the 3mm pixel size SiPM and using the Anger technique.
Source: Own source.

c) Position reconstruction along the X direction of a gamma-ray impinging in the corner of the crystal, for the 3mm pixel size SiPM and using the Anger technique.
Source: Own source.

Fig. 29 Spatial reconstruction of gamma-ray interaction points along the detector's diagonal using the Anger technique.
Source: Own source.

Fig. 30 a) Position reconstruction along the X direction of a gamma-ray impinging in the centre of the crystal, for the 1mm pixel size SiPM and using the Pani technique.
Source: Own source.

b) Position reconstruction along the X direction of a gamma-ray impinging in the centre of the crystal, for the 3mm pixel size SiPM and using the Pani technique.
Source: Own source.

c) Position reconstruction along the X direction of a gamma-ray impinging in the centre of the crystal, for the 3mm pixel size SiPM and using the Pani technique.
Source: Own source.

Fig. 31 a) Position reconstruction along the X direction of a gamma-ray impinging in the corner of the crystal, for the 1mm pixel size SiPM and using the Pani technique.
Source: Own source.

b) Position reconstruction along the X direction of a gamma-ray impinging in the corner of the crystal, for the 3mm pixel size SiPM and using the Pani technique.
Source: Own source.

c) Position reconstruction along the X direction of a gamma-ray impinging in the corner of the crystal, for the 3mm pixel size SiPM and using the Pani technique.
Source: Own source.

Fig. 32 Comparison of two distributions obtained for three photons reaching two photosensors with different pixilation granularity.
Source: Own source.

Fig. 33 Spatial reconstruction of the gamma-ray interaction points along the detector's diagonal using the Pani technique.
Source: Own source.

BIBLIOGRAPHY

- [1] M. C. Moxon and E. R. Rae, "A gamma-ray detector for neutron capture cross-section measurements," *Nuclear Instruments and Methods*, vol. 24, pp. 445-455, 1963.
- [2] R. L. Macklin and J. H. Gibbons, "Capture-Cross-Section Studies for 30-220-keV Neutrons Using a New Technique," *Physical Review*, vol. 159, no. 4, pp. 1007-1012, 20 07 1967.
- [3] F. Corvi, A. Prevignano, H. Liskien and P. B. Smith, "An experimental method for determining the total efficiency and the response function of a gamma-ray detector in the range 0.5-10 MeV," *Nuclear Instruments and Methods in Physics Research A*, vol. 265, no. 3, pp. 475-484, 1988.
- [4] U. Abbondano et al., "New experimental validation of the pulse height weighting technique for capture cross-section measurements," *Nuclear Instruments and Methods Section A*, vol. 521, no. 2, pp. 454-467, 2004.
- [5] C. Domingo-Pardo, "i-TED: A novel concept for high sensitivity (n, γ) cross-section measurements," *Nuclear Instruments and Methods in Physics Research Section A*, vol. 825, pp. 78-86, 2016.
- [6] D. L. Pérez Magán et al., "First tests of the applicability of γ -ray imaging for background discrimination in time-of-flight neutron capture measurements," *Nuclear Instruments and Methods in Physics Research Section A*, vol. 823, pp. 107-119, 2016.
- [7] C. Guerrero et al., "Performance of the neutron time-of-flight facility n_TOF at CERN," *The European Physical Journal A*, vol. 49, pp. 1-15, 2013.
- [8] A. Ulyanov et al., "Localisation of gamma-ray interaction points in thick monolithic CeBr₃ and LaBr₃:Ce scintillators," *Nuclear Instruments and Methods Section A*, vol. 844, pp. 81-89, 2017.
- [9] P. G. Thirolf et al., "A Compton camera prototype for prompt gamma medical imaging," *EPJ Web of Conferences*, vol. 117, no. 05005, 2016.
- [10] G. Oddo, "Die Molekularstruktur der radioaktiven Atome," *Zeitschrift für anorganische Chemie*, vol. 87, no. 1, pp. 253-268, 1914.
- [11] W. D. Harkins, "THE EVOLUTION OF THE ELEMENTS AND THE STABILITY OF COMPLEX ATOMS. I. A NEW PERIODIC SYSTEM WHICH SHOWS A RELATION BETWEEN THE ABUNDANCE OF THE ELEMENTS AND THE STRUCTURE OF THE NUCLEI OF ATOMS.," *Journal of the American Chemical Society*, vol. 39, no. 5, p. 856879, 1917.
- [12] V. M. Goldschmitz, *Geochemische Verteilungsgesetze der Elemente. ix Die Mengenverhältnisse der Elemente und der Atomarten*, Oslo, 1938.
- [13] R. A. Alpher, H. Bethe and G. Gamow, "The origin of chemical elements," *Physical Review*, vol. 73, no. 7, p. 803, 1948.

- [14] R. A. Alpher and R. C. Herman, "Theory of the Origin and Relative Abundance Distribution of the Elements," *Reviews of Modern Physics*, vol. 22, no. 2, pp. 153-212, 1950.
- [15] P. W. Merrill, "Technetium in the stars," *Science*, vol. 479, no. 89, p. 484, 1952.
- [16] E. M. Burbidge, G. R. Burbidge, W. A. Fowler and F. Hoyle, "Synthesis of the Elements in Stars," *Reviews of Modern Physics*, vol. 29, no. 4, pp. 547-650, 1957.
- [17] A. G. Cameron, Stellar evolution, nuclear astrophysics, and nucleogenesis, Atomic energy of Canada Limited, 1957.
- [18] F. Käppeler et al., "The s process: Nuclear physics, stellar models and observations," *Reviews of Modern Physics*, vol. 83, no. 1, pp. 157-193, 2011.
- [19] "The s-Process," [Online]. Available:
<https://ned.ipac.caltech.edu/level5/Sept01/Meyer/Meyer4.html>.
- [20] P. A. Seeger et al, "Nucleosynthesis of Heavy Elements by Neutron Capture," *Astrophysical Journal Supplement*, vol. 11, p. 121, 1965.
- [21] D. Clayton and R. A. Ward, "S-Process Studies: Exact Evaluation of an Exponential Distribution of Exposures," *Astrophysical Journal*, vol. 193, pp. 397-400, 1974.
- [22] J. Sánchez Rojo, "El proceso-s de captura de neutrones en las estrellas de la rama asintótica de las gigantes.," Universidad Complute Madrid, 2016.
- [23] S. Alzubaidi, "The Frankfurt neutron source FRANZ," *The European Physical Journal Plus*, 2016.
- [24] A. Bensussan, "GELINA: A modern accelerator for high resolution neutron time of flight experiments," *Nuclear Instruments and Methods*, vol. 155, no. 1, pp. 11-23, 1978.
- [25] K. H. Guber et al., "Recent refurbishment of the Oak Ridge Electron Linear Accelerator neutron source," in *Internationa Conference on Nuclear Data for Science and Technology 2007*, 2008.
- [26] P. E. Koehler, "Comparison of white neutron sources for nuclear astrophysics experiments using very small samples," *Nuclear Instruments and Methods in Physics Research Section A*, vol. 460, no. 2, pp. 352-361, 2001.
- [27] P. W. Lisowski, "The Los Alamos National Laboratory Spallation Neutron Sources.," *Nuclear Science and Engineering*, vol. 106, no. 2, 1990.
- [28] S. Sawada, "J-PARC, Japan Proton Accelerator Research Complex," *Nuclear Physics A*, vol. 782, no. 1, pp. 434-441.
- [29] C. Guerrero et al., "The n_TOF Total Absorption Calorimeter for neutron capture measurements at CERN," *Nuclear Instruments and Methods in Physics Research Section A*, vol. 608, no. 3, pp. 424-433, 2009.

- [30] F. Voss et al., "Stellar neutron capture cross sections for Pr and Dy isotopes," *Physical Review C (Nuclear Physics)*, vol. 59, no. 2, pp. 1154-1170, 1999.
- [31] K. Wisshak et al., "Stellar neutron capture cross sections of the Lu isotopes," *Physical Review C*, vol. 73, no. 1, p. 015807, 2006.
- [32] M. Asplund et al., "The Chemical Composition of the Sun," *Annual Review of Astronomy and Astrophysics*, vol. 47, pp. 481-522, 2009.
- [33] C. Arlandini et al., "Neutron Capture in Low-Mass Asymptotic Giant Branch Stars: Cross Sections and Abundance Signatures," *The Astrophysical Journal*, vol. 525, pp. 886-900, 1999.
- [34] A. Borella et al., "High-resolution neutron transmission and capture measurements of the nucleus ^{206}Pb ," *Physical Review C*, vol. 76, p. 014605, 2007.
- [35] L. Pasquini et al., "Installation and commissioning of FLAMES, the VLT Multifibre Facility," *The Messenger*, vol. 110, pp. 1-9, 2002.
- [36] C. Chiappini et al., "Imprints of fast-rotating massive stars in the Galactic Bulge," *Nature*, vol. 474, pp. 454-457, 2011.
- [37] U. Abbondanno et al., "Neutron Capture Cross Section Measurement of ^{151}Sm at the CERN Neutron Time of Flight Facility (n_TOF)," *Physical Review Letters*, vol. 93, no. 16, p. 161103, 2004.
- [38] C. Lederer et al., "Neutron Capture Cross Section of Unstable ^{63}Ni : Implications for Stellar Nucleosynthesis," *Physical Review Letters*, vol. 110, no. 2, p. 022501, 2013.
- [39] P. Zugec et al., "GEANT4 simulation of the neutron background of the C6D6 set-up for capture studies at n_TOF," *Nuclear Instruments and Methods in Physics Research Section A*, vol. 760, pp. 57-67, 2014.
- [40] G. Tagliente et al., "The ^{93}Zr reaction up to 8 keV neutron energy," *Physical Review C*, vol. 87, no. 1, p. 014622, 2013.
- [41] P. Neyskens, "The temperature and chronology of heavy-element synthesis in low-mass stars," *Nature*, vol. 517, no. 7533, pp. 174-176, 2015.
- [42] "Wikipedia (Compton Scattering)," [Online]. Available: https://en.wikipedia.org/wiki/Compton_scattering.
- [43] S. Wilderman et al., "Fast algorithm for list mode back-projection of Compton scatter camera data," in *1997 IEEE Nuclear Science Symposium Conference Record*, Albuquerque, NM, 1997.
- [44] L. Mihailescu et al., "SPEIR: A Ge Compton camera," *Nuclear Instruments and Methods in Physics Research Section A*, vol. 570, no. 1, pp. 89-100, 2007.
- [45] J. Roser Martínez, "Study of Compton imaging sensitivity to intrinsic detector performance," Universitat de València, València, 2017.

- [46] "Beijin Scitlion Technology Corp., LTD," [Online]. Available: <http://www.scitlion.com/>.
- [47] O. Guillot-Noël et al., "Optical and scintillation properties of cerium-doped LaCl₃, LuBr₃ and LuCl₃," *Journal of Luminescence*, vol. 85, pp. 21-35, 1999.
- [48] "PETsys Electronics," [Online]. Available: <http://www.petsyselectronics.com/web/>.
- [49] A. Di Francesco et al., "TOFPET2: a high-performance ASIC for time and amplitude measurements of SiPM signals in time-of-flight applications," *Journal of Instrumentation*, vol. 11, 2016.
- [50] "Integrating ADC (Wikipedia)," [Online]. Available: https://en.wikipedia.org/wiki/Integrating_ADC.
- [51] K. Shimazoe et al., "Dynamic Time Over Threshold Method," *IEEE Transactions on Nuclear Science*, vol. 59, no. 6, pp. 3213-3217, 2012.
- [52] G. F. Knoll, *Radiation Detection and Measurement*, Wiley, 2010.
- [53] S. Agostinelli et al., "Geant4—a simulation toolkit," *Nuclear Instruments and Methods in Physics Research Section A*, vol. 506, no. 3, pp. 250-303, 2003.
- [54] P. Gumplinger, "Optical Photon Processes in GEANT4," 2002.
- [55] E. Dietz-Laursonn, "Peculiarities in the Simulation of Optical Physics with Geant4," 2016.
- [56] M. Janecek, "Simulating Scintillator Light Collection Using Measured Optical Reflectance," *IEEE Transactions on Nuclear Science*, vol. 57, no. 3, pp. 964-970, 2010.
- [57] R. Brun, "ROOT — An object oriented data analysis framework," *Nuclear Instruments and Methods in Physics Research Section A*, vol. 389, no. 1, pp. 81-86, 1997.
- [58] C. W. Lerche et al., "Depth of γ -ray interaction within continuous crystals from the width of its scintillation light-distribution," *IEEE Transactions on Nuclear Science*, vol. 52, no. 3, pp. 560-572, 2005.
- [59] A. Bethe and C. Critchfield, "The Formation of Deuterons by Proton Combination," *Physical Review*, vol. 54, pp. 248-254, 1938.
- [60] H. A. Bethe, "Energy Production in Stars," *Physical Review*, vol. 55, no. 5, pp. 434-456, 1939.
- [61] C. F. von Weizsäcker, "Über Elementumwandlungen in Innern der Sterne II," *Physikalische Zeitschrift*, vol. 39, pp. 633-646, 1938.
- [62]